Determination of Convective Boundary Layer Entrainment Fluxes, Dissipation Rates, and the Molecular Destruction of Variances: Theoretical Description and a Strategy for Its Confirmation with a Novel Lidar System Synergy

VOLKER WULFMEYER

Institute of Physics and Meteorology, University of Hohenheim, Stuttgart, Germany, and Cooperative Institute for Research in Environmental Sciences, Boulder, Colorado

SHRAVAN KUMAR MUPPA, ANDREAS BEHRENDT, EVA HAMMANN, AND FLORIAN SPÄTH

Institute of Physics and Meteorology, University of Hohenheim, Stuttgart, Germany

ZBIGNIEW SORBJAN

Physics Department, Marquette University, Milwaukee, Wisconsin

DAVID D. TURNER

NOAA/National Severe Storms Laboratory, Norman, Oklahoma

R. MICHAEL HARDESTY

NOAA/Earth System Research Laboratory, Boulder, Colorado

(Manuscript received 22 December 2014, in final form 20 October 2015)

ABSTRACT

Atmospheric variables in the convective boundary layer (CBL), which are critical for turbulence parameterizations in weather and climate models, are assessed. These include entrainment fluxes, higher-order moments of humidity, potential temperature, and vertical wind, as well as dissipation rates. Theoretical relationships between the integral scales, gradients, and higher-order moments of atmospheric variables, fluxes, and dissipation rates are developed mainly focusing on the entrainment layer (EL) at the top of the CBL. These equations form the starting point for tests of and new approaches in CBL turbulence parameterizations. For the investigation of these relationships, an observational approach using a synergy of ground-based water vapor, temperature, and wind lidar systems is proposed. These systems measure instantaneous vertical profiles with high temporal and spatial resolution throughout the CBL including the EL. The resolution of these systems permits the simultaneous measurement of gradients and fluctuations of these atmospheric variables. For accurate analyses of the gradients and the shapes of turbulence profiles, the lidar system performances are very important. It is shown that each lidar profile can be characterized very well with respect to bias and system noise and that the constant bias has negligible effect on the measurement of turbulent fluctuations. It is demonstrated how different gradient relationships can be measured and tested with the proposed lidar synergy within operational measurements or new field campaigns. Particularly, a novel approach is introduced for measuring the rate of destruction of humidity and temperature variances, which is an important component of the variance budget equations.

1. Introduction

The turbulent transport of heat, matter, and momentum in the convective boundary layer (CBL) is essential for many key processes in the atmosphere. It determines the horizontal and vertical distribution of scalars such as humidity and other constituents as well as the vertical

Denotes Open Access content.

Corresponding author address: Volker Wulfmeyer, Institute of Physics and Meteorology, University of Hohenheim, Garbenstraße 30, 70599 Stuttgart, Germany.
E-mail: volker.wulfmeyer@uni-hohenheim.de

DOI: 10.1175/JAS-D-14-0392.1

stability. Particularly critical are the entrainment fluxes at the CBL top, as they influence the 3D fields of water vapor, temperature, and horizontal wind in the lower troposphere in both vertical directions: above the CBL by entrainment processes and from the CBL top down to the surface and the soil–vegetation layers by its coupling with the surface fluxes and the closure of the surface energy balance. The resulting 3D fields characterize the preconvective environment and influence thunderstorm initiation as well as the development of clouds and precipitation.

Generally, the grid increments of state-of-the-art weather forecast and climate models are too large to resolve small-scale boundary layer turbulence. Consequently, turbulence parameterizations (TP) are essential components of almost all weather and climate models. To a great extent, the TP determines the quality of the simulation of land surface–atmosphere feedback (e.g., Milovac et al. 2014). A particular weakness of the models is the parameterization of entrainment fluxes, which is required for a high quality of simulations on all time scales. On short time scales, an incorrect simulation of entrainment leads to erroneous evolutions of CBL moisture and temperature as well as the convective available potential energy and convective inhibition, which results in poor skill of predicting convection initiation. On longer time scales, incorrect entrainment fluxes cause errors in the vertical distribution of water vapor with negative consequences for the simulation of climate statistics with respect to radiative transfer and the evolution of clouds and precipitation. This concerns reanalyses, regional dynamical downscaling, and global climate change projections. The high sensitivity of NWP model forecast quality on the CBL TP was demonstrated by, for example, Hong et al. (2006), Hill and Lackmann (2009), and Xie et al. (2012) and with respect to the performance of regional climate models by, for example, Dethloff et al. (2001), Park and Bretherton (2009), and Samuelsson et al. (2011).

Models for entrainment fluxes were derived in various publications (Van Zanten et al. 1999; Fedorovich et al. 2004), and relationships useful for applications in NWP models were proposed (Noh et al. 2003). For instance, in the nonlocal Yonsei University (YSU) TP (Hong et al. 2006), the water vapor entrainment flux is the product of an entrainment velocity and the moisture jump at the CBL top. The entrainment velocity is estimated by assuming a constant ratio between the surface and the entrainment heat fluxes of -0.15 and by diagnosing the temperature jump at the CBL top. However, it is unclear whether this constant ratio holds in a real atmospheric boundary layer where gravity waves and wind shear are expected to have a great influence on entrainment fluxes (Wulfmeyer 1999a; Conzemius and Fedorovich 2006). Particularly, it is expected that the temperature flux ratio decreases to approximately -0.3 during shear convection and even more during forced convection with dramatic consequences on moistening or drying conditions (Sorbjan 2005, 2006).

Sorbjan (2001, 2005, 2006) developed CBL scaling laws for deriving profiles of fluxes and higher-order moments of atmospheric variables. These scaling approaches relate fluxes and higher-order moments of atmospheric variables to their gradients in the entrainment layer (EL). Furthermore, these relationships include dependencies of fluxes and variances on the gradient Richardson number so that the influence of wind shear can also be included. If these relationships are valid, simple tests of existing TPs will be possible.

Advanced CBL TPs with refined representation of entrainment may be derived and incorporated in mesoscale models. This will be possible for hierarchies of model simulations from relatively coarse grid increments to the gray zone (e.g., Saito et al. 2013) where turbulent fluctuations become resolved. Gray-zone experiments are a very important area of research, as both regional climate models and NWP models will reach the corresponding grid increments on the order of 1 km within the next years. Therefore, the representation of land–atmosphere feedback of this new model generation has to be studied in great detail and to be optimized, including a realistic simulation of clouds and precipitation.

A prerequisite of the application of new scaling relationships is their verification. This can be realized by performing large-eddy simulations (LESs) and the confirmation of their results by dedicated observations. Since the 1970s, LES has been used for studying the CBL under various conditions (Deardorff 1970). Advances in computing power and model developments enable the resolution of turbulence above the surface layer throughout the CBL including the EL. Most of the runs have been performed under strong convective conditions with homogeneous surface heat fluxes (Wyngaard and Brost 1984). The results were used for deriving parameterizations of fluxes and variances (Moeng and Sullivan 1994; Ayotte et al. 1996) and their dependence on varying strengths of the inversion (Sorbjan 1996). Detailed studies of entrainment processes were presented by Sullivan et al. (1998) and Kim et al. (2003). First studies are available considering the heterogeneity of surface fluxes (Maronga and Raasch 2013). The similarity relationships derived in Sorbjan (2005, 2006) were tested by only a few dedicated LESs so that it is still not clear whether these relationships are generally applicable.

However, it must be considered that most of the LES results introduced above were based on periodic

boundary conditions, homogeneous land surface conditions, and specific assumptions of the interaction of the free troposphere (damping layers) with the CBL. Effects of land surface heterogeneity, interaction of gravity waves with CBL turbulence, wind shear in the EL, inversion strengths, and large-scale forcing have often not been considered in detail. Only a few studies considering realistic heterogeneous surface were performed (e.g., Hechtel et al. 1990; Maronga and Raasch 2013) and these were used primarily to study the surface energy balance closure problem (Kanda et al. 2004). Thus, more realistic LES studies are still required, for example, by nesting them in mesoscale environments or by gray-zone experiments of limited area or even with global models.

Further progress has recently been achieved by the direct numerical simulation (DNS) of entrainment processes (e.g., Waggy et al. 2013; Garcia and Mellado 2014). These results have been applied to derive further insight in the dependence of entrainment velocities, variances, and fluxes as well as eddy diffusivity on scaling variables. Similar to LES, additional studies are required to study the validity of DNS results in inhomogeneous terrain and in dependence of the mesoscale environment.

Models are only as good as the data used for their verification. The only way to confirm similarity relationships, LES, and DNS of turbulent transport and exchange processes are observations with sufficient resolution and accuracy. This verification should be performed under a range of different meteorological conditions, both at the surface and throughout the mixed layer (ML) and the EL. The observations should provide not only measurements of profiles and gradients of atmospheric variables but also their turbulent fluctuations. Reaching the CBL top is possible with aircraft in situ or remote sensing instrumentation as well as ground-based, vertically steering, or scanning lidar or clear-air radar systems. Unfortunately, dedicated observations for studying LES and TPs are relatively sparse. Still, to date, most of the studies were performed using aircraft in situ turbulence sensors (e.g., Lenschow et al. 1994). Here, it is very challenging to derive instantaneous profiles of turbulent quantities owing to sampling issues and complex flight patterns with the operation of in situ sensors only. Furthermore, it is difficult to measure the distance between the flight lag and the CBL depth z_i, which is important to parameterize variables as functions of z/z_i (e.g., Turner et al. 2014a). Aircraft equipped with lidar systems flying close to the CBL top can deliver both vertical profiles and measurements of the spatial inhomogeneities (Crum and Stull 1987; Crum et al. 1987; Kiemle et al. 1997; Couvreux et al. 2005). However, aircraft campaigns are expensive and relatively sparse so that it is difficult to relate the results to a variety of meteorological conditions. Mounting in situ sensors on tethered balloons may be another option but it is challenging to reach the CBL top, which can typically range up to 2000 m or more in some locations.

Therefore, for turbulence studies, it is worthwhile to apply a synergy of in situ measurements with airborne and ground-based remote sensing. Passive remote sensing systems such as Fourier-transform infrared (FTIR) (Turner and Löhnert 2014) spectroscopy and microwave radiometers (MWRs) (Löhnert et al. 2009) demonstrated great potential for ABL profiling. However, the vertical resolution of the retrievals, which are based on the inversion of the radiative transfer equation, is limited by the width of weighting functions to 500 m or more in the EL so that gradients of humidity and temperature are mostly averaged out (Wulfmeyer et al. 2015a). Furthermore, the retrievals are generally too noisy for resolving turbulent fluctuations (Kalthoff et al. 2013).

Clear-air radars observe either the refractive index structure parameter or reflectivity from insects (Emeis 2011). These features can be used to retrieve line-of-sight wind velocities or vertical wind speed. Clear-air radar does not provide direct measurements of wind speed because, in the case of structure parameter measurements, the first moment of the Doppler spectrum is influenced by covariances between reflectivity and radial velocity fluctuations (Muschinski and Sullivan 2013). Nevertheless, volume imaging of wind fields is possible with a resolution of a few seconds (e.g., Mead et al. 1998). In the case of insect backscatter, it is questionable whether these can be considered as tracers for atmospheric motion. Therefore, cloud radar signals are usually not evaluated with respect to wind speed in the clear CBL but in clouds.

The relation between the refractive index structure parameter and temperature and moisture gradients can also be applied for retrieving temperature and moisture profiles (Tsuda et al. 2001). However, this method relies on additional reference measurements of humidity and knowledge of the sign of the refractive index gradient so that its accuracy is limited and routine application is difficult. For temperature profiling, the radar acoustic sounding system (RASS) has been developed (e.g., Matuura et al. 1986). These systems measure the propagation speed of sound so that it is possible to retrieve the virtual temperature profile. This technique is limited by the altitude coverage when high horizontal winds carry the sound waves outside of the radar beam. Nevertheless, in the CBL, measurements of temperature profiles with turbulence resolution have been demonstrated (Angevine et al. 1993; Wulfmeyer 1999a).

Lidar systems measure range-resolved signals, which are directly related to atmospheric dynamics and thermodynamics. Thus, these have a great potential for deriving gradients and turbulent fluctuations of humidity, temperature, and wind, simultaneously. For decades, Doppler lidar (DL) systems, which measure the Doppler shift of aerosol particle backscatter by heterodyne detection, have been used for the profiling of higher-order turbulent moments of vertical wind and turbulent kinetic energy dissipation rate (Frehlich et al. 1998; Lenschow et al. 2000; Frehlich and Cornman 2002; Wulfmeyer and Janjić 2005; Hogan et al. 2009; Lothon et al. 2009; Tucker et al. 2009; Ansmann et al. 2010; Träumner et al. 2011; Lenschow et al. 2012). The routine operation of Doppler lidar systems is now possible, as these systems are commercially available and affordable from various companies.

With respect to water vapor profiling, two different lidar options are available. These are water vapor differential absorption lidar (WVDIAL) or water vapor Raman lidar (WVRL), which both can measure profiles and gradients of absolute humidity or mixing ratio as well as turbulent moments in the CBL (Wulfmeyer 1999b; Wulfmeyer et al. 2010; Turner et al. 2014a,b; Muppa et al. 2015). Combinations of these systems have been applied for ground-based profiling of the latent heat flux (Senff et al. 1994; Wulfmeyer 1999a; Giez et al. 1999; Linné et al. 2007; Behrendt et al. 2011) and higher-order moments (Wulfmeyer 1999b; Lenschow et al. 2000). The high accuracies and turbulence resolutions of WVDIAL and Doppler lidar from aircraft have also been used for latent heat flux profiling (Kiemle et al. 2007, 2011) and for detailed comparisons with LES (Couvreux et al. 2005, 2007). Particularly exciting is the fact that recently temperature rotational Raman lidar (TRRL) reached the resolution needed for temperature turbulence profiling as well (Hammann et al. 2015; Behrendt et al. 2015).

In this work, we are focusing on the capabilities and performances of ground-based lidar systems of this kind because these have the advantage that they can provide continuous profiling of mean profiles, gradients, and turbulence profiles improving sampling statistics during similar meteorological conditions. These systems are becoming available in different climate regimes: at the Atmospheric Radiation Measurement (ARM) Program Southern Great Plains site in Oklahoma, United States; in tropical regions such as the ARM site in Darwin, Australia (www.arm.gov/sites; operated from December 2010 until December 2014; Ackerman and Stokes 2003; Mather and Voyles 2013); and in the midlatitudes at various observatories such as Lindenberg, Germany, and Cabauw, the Netherlands; as well as during field campaigns such as the Convective and Orographically-induced Precipitation Study (COPS) (Wulfmeyer et al. 2008, 2011) (www.uni-hohenheim.de/cops), the High Definition Clouds and Precipitation [HD(CP)^2] Observational Prototype Experiment (HOPE) (https://hdcp2.zmaw.de), and the recent Surface Atmospheric Boundary Layer Exchange (SABLE) campaign (Wulfmeyer et al. 2015b).

We demonstrate that this novel synergy of lidar systems consisting of DL, WVDIAL/WVRL, and TRRL provides a complete dataset of gradients and turbulent moments for the verification of LES and similarity relationships. We focus on ground-based observations, as it is possible to deploy these lidar systems very close to each other for simultaneous measurements of covariances between different atmospheric variables. Furthermore, measurements can be collected under a variety of different conditions producing robust statistics of turbulent quantities in an affordable manner.

This study is organized as follows: In section 2, we derive an advanced set of scaling relationships in the CBL. Particularly, we derive relationships of momentum, latent heat, and sensible heat fluxes as well as higher-order moments to mean wind, temperature, and moisture gradients with particular emphasis on the EL. Furthermore, new equations for relating integral scales to turbulent quantities are derived. Particularly, what is to our knowledge for the first time, a novel technique for measuring the molecular destruction rates of water vapor and temperature variances is developed that are important components of the variance budget equations.

In section 3, we analyze the capabilities of DL, WVDIAL, WVRL, and TRRL for profiling vertical wind, water vapor, and temperature as well as their higher-order moments. We show how the lidar measurements can be combined for deriving fluxes and higher-order moments using measurements of vertical gradients of mean profiles. The results demonstrate that the proposed lidar synergy is necessary but also sufficient for providing a complete set of measurements for studying and verifying the proposed similarity relationships. It is also shown that these synergetic lidar measurements open up new possibilities for thorough comparisons with LES and detailed studies of TPs.

In section 4, we present first results using WVDIAL and TRRL for studying turbulence profiles up to the third order and their relationship to water vapor and temperature gradients as well as entrainment fluxes. We also get first insight into molecular destruction rates.

In section 5, the results are summarized. A series of new field campaigns in different climate regions is proposed as contributions to studies of land–atmosphere

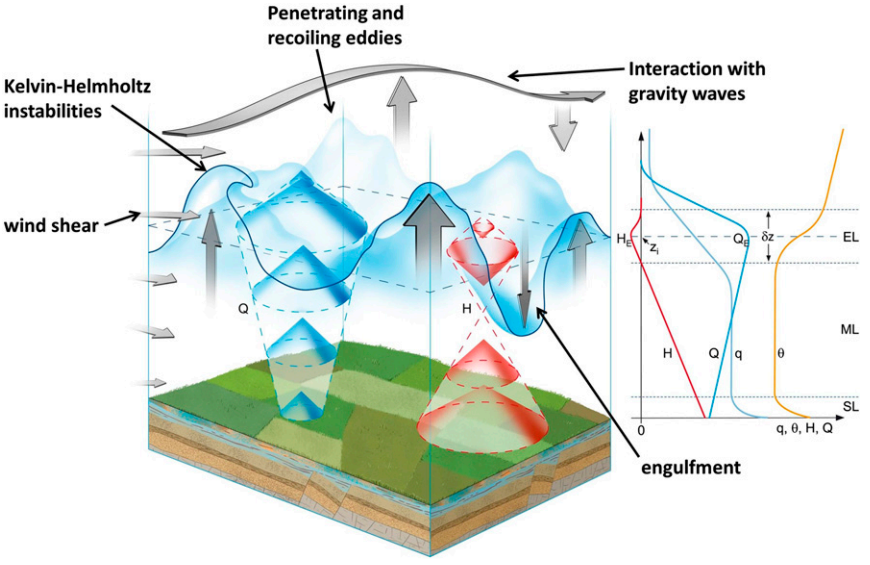

FIG. 1. The convective boundary layer: vertical structure and key processes. The cones on the left side of the figure indicate the mean direction (arrows) and the mean strength (diameters) of either the sensible heat (red) or the latent heat (blue) fluxes.

interaction as well as theories and parameterizations of turbulence in the CBL. In the appendix, the sensitivity of the results on systematic and noise errors is investigated and it is confirmed that the current state-of-the-art lidar systems are able to measure profiles and moments with high accuracy and resolution.

2. Convective boundary layer structure and entrainment

a. *Vertical structure*

The vertical structure and the turbulent activity of the CBL is depicted in Fig. 1. In a horizontally homogeneous, quasi-stationary, and well-mixed CBL it is expected that the mean potential temperature θ profile can be characterized by a negative gradient in the surface layer (SL), a constant in the ML, and an increase in the EL due to the temperature inversion.

Here, we define the entrainment zone as the region, in which a nonturbulent fluid from the free troposphere is mixed into the CBL and remains part of the CBL afterward. This can occur far downward in the CBL by engulfment, as often observed by remote sensing systems. In contrast, the EL or the interfacial layer is the region around the inversion at the CBL top, which can be used to locate the instantaneous and mean gradients as well as the mean entrainment flux (LeMone 2002).

In the SL, the mean specific humidity q profile should have a negative gradient as well, as long as significant evapotranspiration is present, a slight negative gradient in the ML, and a stronger negative gradient in the EL. Well-mixed conditions are usually achieved after threefold to fourfold eddy turnover time or the CBL time scale $t^* \approx z_i/w_*$, where z_i is the mean CBL depth and w_* the convective velocity scale:

$$w_* = \left(\frac{G}{\overline{\theta}_v} z_i H_{v,0}\right)^{1/3}. \tag{1}$$

Here, G is the acceleration due to gravity, $\overline{\theta}_v$ is the mean virtual potential temperature in the CBL, and $H_{v,0}$ is surface buoyancy flux. Typical values of w_* in a well-developed CBL range between approximately 1 and 2 m s^{-1}.

In the absence of significant horizontal advection, the evolutions of θ and q are driven by the vertical divergences of the sensible and latent heat flux profiles (H and Q), respectively. Their absolute mean values and directions (the spectra and sizes are not shown) are indicated in Fig. 1 by the diameters and the directions of the cones, respectively. Whereas $H(z)$ must have a negative slope reaching a negative value in the EL, $Q(z)$ can have a negative or positive slope depending on whether the difference between the entrainment flux Q_E and the surface flux Q_0 is negative or positive. In any case, as long as there is a negative slope of q in the EL, then $Q_E > 0$. The understanding and the parameterization of these flux divergences—also for momentum—is the essence of TPs, which are fundamental for weather and climate modeling.

In the SL, the vertical stability can be characterized by the bulk Richardson number,

$$\mathrm{Ri}_b = \frac{G}{\theta_a} z \frac{\theta_{va} - \theta_{vg}}{U_{\mathrm{SL}}^2}, \tag{2}$$

where θ_a is the potential temperature in the surface layer; z is height above the displacement height in the canopy or in other land cover; θ_{va} and θ_{vg} are the virtual potential temperatures of the air and the land surface, respectively; and U_{SL} is the horizontal wind speed in the SL at height z. The depth of the SL can be defined by the extent to which the vertical change of fluxes is less than 10%. Over a homogeneous surface, the resulting vertical profiles of wind, temperature, and humidity can be described by the Monin–Obukhov similarity theory (MOST), which relates their gradients to surface fluxes and stability functions given for different ranges of Ri_b (Grachev et al. 2000; Poulos et al. 2002; Jiménez et al. 2012). The study and measurements of these relationships in the surface layer is possible by using scanning lidar systems and eddy covariance instrumentation and is subject of future publications.

In the ML, θ is nearly constant with height, indicating a well-mixed boundary layer. Vertical flux profiles are evolving in time and are well defined for a specific domain and time average. This can be studied by deriving integral length and temporal scales for the higher moments of the atmospheric variables and their covariances, which can be related to their sampling errors (Lenschow et al. 1994). Typically, 30–60-min averaging time is needed for deriving profiles of turbulent quantities with low noise and acceptable sampling errors on the order of 10%–20%. However, this averaging time may increase further at lower horizontal wind speed U. The amount and the gradient of q are strongly dependent on the ratio between the fluxes in the SL and the EL. As it is particularly challenging and crucial to derive entrainment fluxes, we will focus on vertical exchange processes in the EL.

b. The entrainment layer

The EL separates the ML from the free troposphere by a temperature inversion. The strength of this inversion and the entrainment flux are the result of a variety of interacting processes. These are indicated in Fig. 1 and are mainly due to four effects: 1) the engulfment of air from the free troposphere mixed downward in the turbulent CBL, 2) instabilities induced by wind shear at the EL interface such as Kelvin–Helmholtz and Holmboe waves, 3) penetrating and recoiling convective eddies, and 4) the propagation and excitation of wave modes such as gravity waves and their interaction with the turbulent eddies.

Consequently, various local and nonlocal processes are contributing to the fluxes, which are neither well understood nor accurately parameterized in state-of-the-art mesoscale models. Therefore, sophisticated theoretical concepts are necessary to understand the turbulent variables in the EL. These concepts have to be verified by new combinations of measurements.

1) Higher-order moments and entrainment fluxes

It can be expected that the flux Q through an interface such as the EL is related to the mean gradient of the variable of interest q so that

$$\mathbf{Q} = -\frac{1}{R}\nabla q, \tag{3}$$

where R is the resistance of the interface. This relationship from stochastic physics is not only used for studying turbulent transport in the atmosphere but also water transport in the soil or fluxes at the land surface (Zehe et al. 2014). The challenge is to relate in a comprehensive and physical way the resistance R to parameters that are expected to influence the entrainment fluxes. Thus, it is desirable to derive a closed set of scaling variables in the EL so that their gradients can be related to fluxes and higher-order turbulent moments. A corresponding set of equations was proposed by Sorbjan (1996, 2001, 2005, 2006) and reads

$$S_w = w_*, \tag{4}$$

$$S_L = \frac{w_*}{N_E}, \tag{5}$$

$$S_\theta = S_L \gamma_E = w_* \frac{\gamma_E}{N_E}, \quad \text{and} \tag{6}$$

$$S_q = S_L g_E = w_* \frac{g_E}{N_E}, \tag{7}$$

where S_w, S_L, S_θ, and S_q are the scaling variables for vertical velocity w statistics, the EL length scale L, the potential temperature θ, and the specific humidity q. The index E denotes that all variables and gradients are taken in the EL. The gradients of θ and q in the EL are γ_E and g_E, respectively. Alternatively, it may be reasonable to replace w_* by the standard deviation of the vertical velocity fluctuations $\sqrt{\overline{w'^2}_E}$, which is easy to do in all following scaling relationships. For now, we stick with the hypothesis that w_* is the appropriate EL scaling variable.

The Brunt–Väisälä frequency N_E depends on the inversion strength in the EL according to

$$N_E = \sqrt{\beta_E \gamma_E}, \tag{8}$$

with the buoyancy parameter $\beta := G/\theta$.

This scaling [Eqs. (4)–(7)] is based on the following assumptions: 1) the turbulent fluctuations of the vertical wind in the EL scale with the buoyant forcing from the land surface and the CBL depth but not with the wind shear, 2) the time scale of fluctuations of atmospheric variables is the inverse of the Brunt–Väisälä frequency, 3) the most important scaling variable for temperature fluctuations is the mean potential temperature gradient at z_i, 4) the most important scaling variable for moisture fluctuations is its mean moisture gradient at z_i, and 5) despite the complex and different physical processes leading to local transport as depicted in Fig. 1, mean but not local gradients remain the most important scaling variables determining the entrainment flux averaged in time or in space over a homogeneous region.

Based on Eqs. (4)–(7), relationships for entrainment fluxes and higher-order moments can be derived. Entrainment fluxes for momentum $M_{u,v,E}$, temperature H_E, and moisture Q_E can be written by the combination of the scaling variables as

$$M_{u,v,E} = -C_M S_L^2 s_E s_{u,v,E} f_M(\mathrm{Ri}_E) = -C_M \left(\frac{w_*}{N_E}\right)^2 s_E s_{u,v,E} f_M(\mathrm{Ri}_E) \equiv -\frac{1}{R_{M,E}} s_{u,v,E}, \quad (9)$$

$$H_E = -C_H S_w S_\theta f_H(\mathrm{Ri}_E) = -C_H w_*^2 \frac{\gamma_E}{N_E} f_H(\mathrm{Ri}_E) \equiv -\frac{1}{R_{H,E}} \gamma_E, \quad \text{and} \quad (10)$$

$$Q_E = -C_Q S_w S_q f_Q(\mathrm{Ri}_E) = -C_Q w_*^2 \frac{g_E}{N_E} f_Q(\mathrm{Ri}_E) \equiv -\frac{1}{R_{Q,E}} g_E, \quad (11)$$

where $M_{u,v,E}$ denotes the momentum fluxes in two horizontal wind directions described by the indices u and v. The constants $C_M, C_H,$ and C_Q are positive and s_E is the wind shear in the EL such that

$$s_E^2 = \left(\frac{du}{dz}\bigg|_E\right)^2 + \left(\frac{dv}{dz}\bigg|_E\right)^2 =: (s_{u,E})^2 + (s_{v,E})^2. \quad (12)$$

By comparing Eqs. (9)–(11) with Eq. (3), indeed resistances with respect to each turbulent flux can be defined. Particularly, we expect that the resistances are functions of the gradient Richardson number

$$\mathrm{Ri}_E = \frac{N_E^2}{s_E^2}, \quad (13)$$

which is conceptually similar to Eq. (2). In shearless conditions (free-convection limit) $s_E \to 0$; thus, $\mathrm{Ri}_E \to \infty$. In this case, the functions $f_{M,H,Q}$ should reach the constant value $\lim_{\mathrm{Ri}_E \to \infty} f_{M,H,Q} = 1$. It may be worthwhile to absorb the constants C_M, C_H, and C_Q in these functions.

For the momentum flux M_E, Sorbjan (2009) analyzed LES datasets and found $C_M \cong 0.2$ and

$$f_M(\mathrm{Ri}_E) = 1 - \frac{1}{\mathrm{Ri}_E}, \quad (14)$$

which is proposed for $\mathrm{Ri}_E > 1$.

For the interfacial heat and humidity fluxes, Sorbjan (2005, 2006) estimated $C_H \cong 0.012$ and $C_Q \cong 0.025$ as well as the dependence of the fluxes on Ri_E by LES and achieved

$$f_{H,Q}(\mathrm{Ri}_E) = \frac{1 + c_{H,Q}/\mathrm{Ri}_E}{\sqrt{1 + 1/\mathrm{Ri}_E}}, \quad (15)$$

where the coefficients $c_{H,Q}$ were assessed to be $c_H \cong c_Q \cong 8$.

In an analogous way, second-order moments of the vertical wind, temperature, and humidity fluctuations can be arranged as follows:

$$\overline{w'^2}_E = C_{w^2} S_w^2 f_{w^2}(\mathrm{Ri}_E) = C_{w^2} w_*^2 f_{w^2}(\mathrm{Ri}_E), \quad (16)$$

$$\overline{\theta'^2}_E = C_{\theta^2} S_\theta^2 f_{\theta^2}(\mathrm{Ri}_E) = C_{\theta^2} w_*^2 \left(\frac{\gamma_E}{N_E}\right)^2 f_{\theta^2}(\mathrm{Ri}_E), \quad \text{and} \quad (17)$$

$$\overline{q'^2}_E = C_{q^2} S_q^2 f_{q^2}(\mathrm{Ri}_E) = C_{q^2} w_*^2 \left(\frac{g_E}{N_E}\right)^2 f_{q^2}(\mathrm{Ri}_E). \quad (18)$$

In the case of EL temperature and humidity variances, Sorbjan (2006) suggested $C_{\theta^2} \cong 0.04$ and $C_{q^2} \cong 0.175$ as well as a functional dependence on Ri_E of the form

$$f_{\theta^2,q^2}(\mathrm{Ri}_E) = \frac{1 + c_{\theta^2,q^2}/\mathrm{Ri}_E}{1 + 1/\mathrm{Ri}_E}. \quad (19)$$

The coefficients c_{θ^2} and c_{q^2} have still to be estimated. For vertical wind, both the function $f_{w^2}(\mathrm{Ri}_E)$ and the coefficient C_{w^2} need to be determined as well.

Figure 2 presents the dependence of the functions f_M, $f_{H,Q}$, and f_{θ^2,q^2} on Ri_E for typical ranges of the proposed constants. The function f_M shows a strong nonlinear behavior for $\mathrm{Ri}_E < 10$ and the momentum flux decreases between $1 < \mathrm{Ri}_E < 10$ by more than an order of magnitude. The other functions show basically three regimes, which may be related to different entrainment processes. In the first regime for $\mathrm{Ri}_E \leq 0.1$, the function f_{θ^2,q^2} is leveling off and approaches the constant value c_{θ^2,q^2}. This may be the range where entrainment is mainly determined by the engulfment of overturning eddies. In contrast, $f_{H,Q}$ is not converging to a limited value but to ∞ for $\mathrm{Ri}_E \to 0$. It is very important to test this different

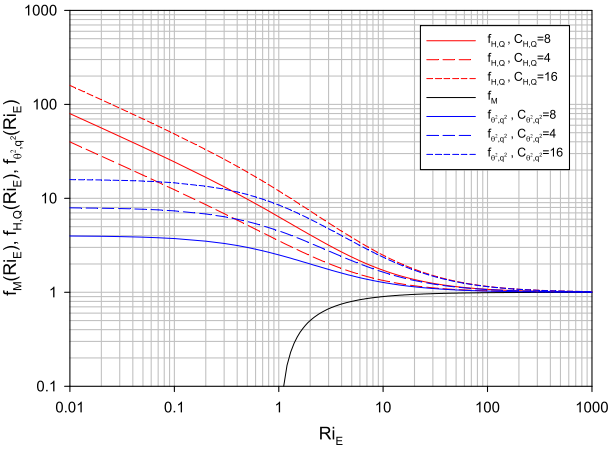

FIG. 2. The functions f_M, $f_{H,Q}$, and f_{θ^2,q^2} for scaling fluxes and variance in dependence of Ri_E. The functions $f_{H,Q}$ and f_{θ^2,q^2} are presented around constants derived by LES.

behavior of the flux and variance scaling functions by additional LES and observations. In the transition regime from $0.1 < \mathrm{Ri}_E < 10$, different processes may be responsible for the strength of entrainment simultaneously. Finally, for $\mathrm{Ri}_E > 10$, both functions $f_{H,Q}$ and f_{θ^2,q^2} are converging to unity and entrainment may mainly be determined by Kelvin–Helmholtz instabilities and interaction with gravity waves. Please note that these results depend on the grid resolution of the corresponding LES. Further refinements are required by LES with increased grid resolution or DNS. It is also important to explore the difference in scaling using Ri_E, which is proposed here and the bulk Richardson number, which was used, for example, in Sullivan et al. (1998) and Träumner et al. (2011).

A similar approach as for the variances may be used to describe the third moments of w', θ', and q' in the EL:

$$\overline{w'^3}_E = C_{w^3} S_w^3 f_{w^3}(\mathrm{Ri}_E) = C_{w^3} w_*^3 f_{w^3}(\mathrm{Ri}_E), \tag{20}$$

$$\overline{\theta'^3}_E = C_{\theta^3} S_\theta^3 f_{\theta^3}(\mathrm{Ri}_E) = C_{\theta^3} w_*^3 \left(\frac{\gamma_E}{N_E}\right)^3 f_{\theta^3}(\mathrm{Ri}_E), \quad \text{and} \tag{21}$$

$$\overline{q'^3}_E = C_{q^3} S_q^3 f_{q^3}(\mathrm{Ri}_E) = C_{q^3} w_*^3 \left(\frac{g_E}{N_E}\right)^3 f_{q^3}(\mathrm{Ri}_E). \tag{22}$$

However, this hypothesis would need to be tested extensively to ensure that the magnitude of the third moments is indeed proportional to the cubes of the gradients for θ and q at z_i as well as to determine the dependence on Ri_E and the coefficients C_{w^3}, C_{θ^3}, and C_{q^3}.

2) Determination of integral scales as well as dissipation and destruction rates

We start with the evaluation of stationary turbulence. This is the case if the time series of the fluctuating variable $q(t)$ can be separated into

$$q(t) = q'(t) + \overline{q(t)}, \tag{23}$$

where $\overline{q(t)}$ is a slowly varying component, which can be derived by low-pass filtering or subtracting a linear trend, and $\overline{q'(t)} = 0$. Of course, this analysis can be performed at each height level in the CBL including the EL; however, for the sake of simplicity we omit an index for the height level in the following. The autocovariance function A of this time series is defined as

$$A_q(t_1, t_2) \equiv \overline{[q(t_1) - \overline{q(t_1)}][q(t_2) - \overline{q(t_2)}]}. \tag{24}$$

If the time series $q(t)$ is stationary then

$$A_q(t_1, t_2) = A_q(t_1 - t_2) = A_q(t_2 - t_1) = A_q(\tau) \tag{25}$$

with $|A_q(\tau)| \le A_q(0)$.

The structure function D of a variable q is defined according to

$$D_q(t_1, t_2) = \overline{[q(t_1) - q(t_2)]^2} \quad \text{or}$$
$$D_q(\tau) = \overline{[q(t+\tau) - q(t)]^2}. \tag{26}$$

If the time series is stationary, it is easy to show

$$D_q(\tau) = 2[A_q(0) - A_q(\tau)] \quad \text{and}$$
$$A_q(\tau) = A_q(0) - 0.5 D_q(\tau). \tag{27}$$

In the spatial domain, the structure function reads

$$D_q(\mathbf{r}_1, \mathbf{r}_2) = \overline{[q(\mathbf{r}_1) - q(\mathbf{r}_2)]^2} \tag{28}$$

and if the field is locally homogeneous and isotropic then

$$D_q(\mathbf{r}_1, \mathbf{r}) = \overline{[q(\mathbf{r}_1 + \mathbf{r}) - q(\mathbf{r}_1)]^2} \equiv D_q(r) \tag{29}$$

and the relations

$$D_q(r) = 2A(0) - 2A_q(r) \quad \text{and}$$
$$A_q(r) = A_q(0) - 0.5 D_q(r) \tag{30}$$

hold.

In the following, we assume that either by high-resolution modeling or measurements, the inertial subrange is resolved for a sufficient short lag of the time series. The inertial subrange lies in between the inner and outer scales of turbulence where it is assumed locally homogeneous and isotropic. Now, we can analyze these equations with respect to the time series of vertical wind, humidity, and temperature at different heights. It was shown in Tatarski (1961) and Monin and Yaglom (1975) that

$$D(r) = C^2 r^{2/3} \tag{31}$$

with the structure parameters C^2 for vertical wind velocity

$$C_w^2 \cong C_K \varepsilon^{2/3}, \tag{32}$$

humidity

$$C_q^2 \cong a_q^2 \frac{\overline{N_q}}{\varepsilon^{1/3}}, \tag{33}$$

and potential temperature

$$C_\theta^2 \cong a_\theta^2 \frac{\overline{N_\theta}}{\varepsilon^{1/3}}, \tag{34}$$

where ε is the turbulent kinetic energy (TKE) dissipation rate, and $\overline{N}_q$ and $\overline{N}_\theta$ are the destruction rates of humidity and potential temperature variances due to molecular processes, respectively. The constants in Eqs. (32)–(34) are considered universal in the inertial subrange. The Kolmogorov constant $C_K \cong 2$ and the constants a_q^2 and a_θ^2 are expected to be in the range 2.8–3.2 (Stull 1988).

Consequently, one way of determining dissipation and destruction rates is to start with the autocovariance function A in the time domain and to assume Taylor's hypothesis of frozen turbulence in the inertial subrange. Then,

$$A_w(\tau) = \overline{w'^2} - \varepsilon^{2/3} U^{2/3} \tau^{2/3}, \tag{35}$$

$$A_q(\tau) = \overline{q'^2} - 0.5 a_q^2 \frac{\overline{N_q}}{\varepsilon^{1/3}} U^{2/3} \tau^{2/3}, \quad \text{and} \tag{36}$$

$$A_\theta(\tau) = \overline{\theta'^2} - 0.5 a_\theta^2 \frac{\overline{N_\theta}}{\varepsilon^{1/3}} U^{2/3} \tau^{2/3}. \tag{37}$$

Using these equations, the atmospheric variance, the dissipation and destruction rates, and the integral scales can be determined, respectively, if the autocorrelation functions and the horizontal wind profile $U(z)$ are known.

This can be shown as follows: all autocovariance functions have the form

$$A(\tau) = \nu_a - k\tau^{2/3}, \tag{38}$$

insofar that distortions by mesoscale variability in the inertial subrange can be neglected. In the following, we assume that this is the case, which can be tested by studying the shape of A for $\tau < \mathscr{T}$, where $\mathscr{T}$ is the integral time scale. If the shapes of the data and the fit agree well, the extrapolation of the structure function fit to the autocovariance data to lag zero yields the atmospheric variance ν_a and the coefficient of the structure function k. This technique separates the atmospheric and the noise variance at lag 0, which is necessary as the latter can often not be neglected [see also the appendix and Eq. (A9)].

The autocorrelation function AC is defined as

$$\mathrm{AC}(\tau) = 1 - \frac{k}{\nu_a}\tau^{2/3}. \tag{39}$$

The root of this equation is

$$\tau_0 = \left(\frac{\nu_a}{k}\right)^{3/2} \tag{40}$$

so that the respective integral time scale can be estimated according to

$$\mathscr{T} = \int_0^{\tau_0} \mathrm{AC}(\tau)\, d\tau = \int_0^{\tau_0} \left(1 - \frac{k}{\nu_a}\tau^{2/3}\right) d\tau, \tag{41}$$

which yields

$$\mathscr{T} = \frac{2}{5}\left(\frac{\nu_a}{k}\right)^{3/2}. \tag{42}$$

Please note that this integration is an approximation of the integral scale of the turbulence fluctuations because we do not integrate to infinity but to the first zero crossing of AC(τ). However, this turned out as a good compromise for separating turbulent fluctuations from mesoscale variability and for getting robust results under the presence of significant system noise (Lenschow et al. 2000; Wulfmeyer et al. 2010; Behrendt et al. 2015).

If the shape of AC is mainly controlled by homogeneous and isotropic turbulence, the ratio between the root and the integral scale gives an estimate of how many lags should be used for the interpolation of the structure function. One natural choice is to take approximately $2\mathscr{T}/\Delta t$ lags, where Δt is the resolution of the time series. If the shape of AC is contaminated by mesoscale variability, then an iteration between the fit of the structure function and the determination of the integral scale may be necessary, resulting in a reduction of the number of lags.

The integration of AC yields the dependence of $\mathscr{T}$ or the integral length scales $\mathscr{R} \cong U\mathscr{T}$ on atmospheric variables:

$$\mathscr{T}_w = \frac{2}{5}\left(\sqrt{\overline{w'^2}}\right)^3 \frac{1}{\varepsilon U}, \quad \mathscr{R}_w = \frac{2}{5}\left(\sqrt{\overline{w'^2}}\right)^3 \frac{1}{\varepsilon}, \tag{43}$$

$$\mathscr{T}_q = \frac{2\sqrt{8}}{5a_q^3}\left(\sqrt{\overline{q'^2}}\right)^3 \sqrt{\frac{\varepsilon}{\overline{N}_q^3}}\,\frac{1}{U},$$

$$\mathscr{R}_q = \frac{2\sqrt{8}}{5a_q^3}\left(\sqrt{\overline{q'^2}}\right)^3 \sqrt{\frac{\varepsilon}{\overline{N}_q^3}}, \quad \text{and} \tag{44}$$

$$\mathscr{T}_\theta = \frac{2\sqrt{8}}{5a_\theta^3}\left(\sqrt{\overline{\theta'^2}}\right)^3 \sqrt{\frac{\varepsilon}{\overline{N}_\theta^3}}\,\frac{1}{U}, \quad \mathscr{R}_\theta = \frac{2\sqrt{8}}{5a_\theta^3}\left(\sqrt{\overline{\theta'^2}}\right)^3 \sqrt{\frac{\varepsilon}{\overline{N}_\theta^3}}. \tag{45}$$

For the vertical wind, its integral time scale is inversely proportional to the dissipation rate and proportional to the 3/2 power of the variance. It can be expected that variance and dissipation are related variables (larger variance leading to larger dissipation), which can be investigated now with our methodology.

In contrast, the integral scales for humidity and potential temperature are proportional to the square root of the TKE dissipation rate and inversely proportional to the 3/2 power of their destruction rates, respectively. The dependence on the variance profiles is the same as for vertical wind. In the future, it will be very interesting to compare the behavior of molecular destruction and TKE dissipation rates and their dependence on various atmospheric conditions. The results can be used for studying the processes controlling their height dependence.

This can be realized in the following way. Combining the fit of the AC functions or the resulting integral scales with the coefficients of the structure functions permits the direct estimation of dissipation rates. For example, for vertical velocity

$$k_w = \varepsilon^{2/3} U^{2/3} \quad \text{and} \tag{46}$$

$$\varepsilon = \frac{k_w^{3/2}}{U} \tag{47}$$

$$= \frac{2}{5} \frac{\left(\sqrt{\overline{w'^2}}\right)^3}{U \mathscr{T}_w} = \frac{2}{5} \frac{\left(\sqrt{\overline{w'^2}}\right)^3}{\mathscr{R}_w}. \tag{48}$$

As the integral scale for vertical wind generally varies less than a factor of 2 with height in the mixed layer and the EL (Lenschow et al. 2000; Lothon et al. 2006), the shape of the ε profile is mainly determined by the profile of the vertical velocity variance.

Correspondingly, for humidity

$$k_q = \frac{1}{2} a_q^2 \frac{\overline{N}_q}{\varepsilon^{1/3}} U^{2/3}, \tag{49}$$

elimination of U with Eq. (47)

$$\frac{k_q}{k_w} = \frac{1}{2} a_q^2 \frac{\overline{N}_q}{\varepsilon}, \tag{50}$$

or elimination of ε with Eq. (47)

$$k_q = \frac{1}{2} a_q^2 \frac{\overline{N}_q}{\sqrt{k_w}} U, \tag{51}$$

thus

$$\overline{N}_q = \frac{2 k_q \sqrt{k_w}}{a_q^2} \frac{1}{U}, \tag{52}$$

or using Eqs. (43) and (44)

$$\overline{N}_q = \frac{4}{5} \frac{\overline{q'^2} \sqrt{\overline{w'^2}}}{a_q^2 \mathscr{T}_q^{2/3} \mathscr{T}_w^{1/3} U} = \frac{4}{5} \frac{\overline{q'^2} \sqrt{\overline{w'^2}}}{a_q^2 \mathscr{R}_q^{2/3} \mathscr{R}_w^{1/3}}. \tag{53}$$

In an analogous way for potential temperature

$$k_\theta = \frac{1}{2} a_\theta^2 \frac{\overline{N}_\theta}{\varepsilon^{1/3}} U^{2/3}, \tag{54}$$

$$\frac{k_\theta}{k_w} = \frac{1}{2} a_\theta^2 \frac{\overline{N}_\theta}{\varepsilon}, \tag{55}$$

$$\overline{N}_\theta = \frac{2 k_\theta \sqrt{k_w}}{a_\theta^2} \frac{1}{U}, \tag{56}$$

or using Eqs. (43) and (45)

$$\overline{N}_\theta = \frac{4}{5} \frac{\overline{\theta'^2} \sqrt{\overline{w'^2}}}{a_\theta^2 \mathscr{T}_\theta^{2/3} \mathscr{T}_w^{1/3} U} = \frac{4}{5} \frac{\overline{\theta'^2} \sqrt{\overline{w'^2}}}{a_\theta^2 \mathscr{R}_\theta^{2/3} \mathscr{R}_w^{1/3}}. \tag{57}$$

Using Eqs. (49) and (54) we achieve

$$\frac{k_q}{k_\theta} \simeq \frac{\overline{N}_q}{\overline{N}_\theta}. \tag{58}$$

Obviously, LES and DNS output or simultaneous measurements of wind, humidity, and potential temperature profiles at high temporal and spatial resolution permit the estimation of the ratio of dissipation rates [Eqs. (50) and (55)] as well as their absolute values [Eqs. (47) and (48), Eqs. (52) and (53), and Eqs. (56) and (57)] provided that accurate measurements of horizontal wind are available. Of course, these equations are only applicable if the conditions of locally homogeneous and isotropic turbulence as well as Taylor's hypothesis are valid.

3) DISCUSSION

For deriving quantitative results, it is essential that all the turbulent quantities introduced above are estimated as accurate and as general as possible. This may be accomplished with turbulence theory, by dedicated LES and DNS studies, and by measurements. As we are not aware of a turbulence theory that permits the derivation of the unknown resistances and dissipation/destruction rates, these relationships need to be tested considering different heterogeneous land surface forcings, stabilities in EL, wind shear, and gravity wave conditions. Furthermore, it is necessary to explore dependencies of fluxes and higher-order moments on different definitions of the Richardson number in the EL and to refine the functional dependence of fluxes and variances on the Richardson number. From the modeling perspective, this requires a chain of mesoscale model simulations

down to the gray zone or the LES scale in order to imbed the model domain with turbulence resolution in a realistic synoptic and mesoscale environment. It is worthwhile to note that the relationships introduced in sections 2b(1) and 2b(2) also provide essential components of CBL energy and water budgets. For instance, dissipation and molecular destruction rates as well as flux divergences are part of these budgets.

Either using idealistic LES and DNS or gray-zone simulations, the results have to be verified by observations. Gradients play an important role in the magnitude of the variances and fluxes, so accurate profiles of horizontal wind, humidity, and potential temperature in the ML, the EL, and the lower free troposphere are critical (Sorbjan 2009). Here, we are focusing on turbulent processes around the EL. So far, particularly in this region, field experiments have not provided suitable datasets that are capable to confirm the complete set of relationships between gradients, variances, fluxes, and dissipation/destruction rates. In the following, we demonstrate that this can be accomplished with a new synergy of lidar systems.

3. Lidar synergy for studying entrainment fluxes as well as dissipation and variance destruction rates

a. Basic observational requirements

To study the relationships between fluxes and gradients [Eqs. (9)–(11)], variances and gradients [Eqs. (16)–(18)], and even higher-order moments [Eqs. (20)–(22)], it is necessary that four conditions are fulfilled: 1) wind, temperature, and humidity profiles must be measured simultaneously with small and height-independent bias in the ML, the EL, and the lower free troposphere; 2) the vertical resolution of the measurements must be high enough to resolve the gradients in the profiles, particularly in the EL; 3) the temporal resolutions of the measurements must be high enough to resolve turbulent fluctuations; and 4) the precision of the measurements must be high enough so that vertical structures in the turbulence profiles can be resolved.

Currently, it is hardly possible to realize this with airborne in situ or remote sensing measurements. Research aircraft with in situ sensors provide measurements of the required variables but only at a specific height level. Therefore, it is difficult to derive a comprehensive dataset of gradient, variance, and flux profiles under different meteorological conditions especially at a range of heights in the ML and the EL. The horizontal and vertical structure of the CBL can be studied by lidar systems deployed on aircraft but these campaigns are sparse and expensive. Another option is a combination of ground-based scanning lidar systems but their development and application is still at its infancy. The height of meteorological towers is generally too low to reach the daytime EL, except special meteorological conditions over land (Zhou et al. 1985), so that these structures also do not come into consideration for deriving comprehensive statistics. Tethered balloons with a combination of in situ sensors may be an option but it will be difficult to get vertical profiles and to reach the CBL top, especially in continental CBLs that can be 2 km deep or more.

Passive infrared and microwave spectrometers may be an approach for retrieving temperature and humidity profiles; however, it has been shown that their temporal and vertical resolution is neither capable of resolving gradients nor turbulent fluctuations in the EL (Wulfmeyer et al. 2015a). In the following, we demonstrate that a synergy of active lidar remote sensing systems with the required vertical and temporal resolutions should be able to provide the desired data.

b. Properties and performance of lidar systems

Recent advances in lidar technology permitted the development of three types of lidar systems, which can measure wind, humidity, and temperature profiles with high resolution and accuracy. The DL can measure either vertical wind profiles in the vertical steering mode or horizontal wind profiles in the velocity azimuth display (VAD or scanning in azimuth at a fixed off-zenith elevation) mode. The signal-to-noise ratio (SNR) of the line-of-sight wind measurements is high enough to reach resolutions of 1 s and 30 m with noise errors on the order of $0.1\,\mathrm{m\,s^{-1}}$. Systematic errors in line-of-sight (LOS) wind measurements are typically on the order of a few centimeters per second. This performance has been demonstrated for decades using research systems like the high-spectral-resolution Doppler lidar (HRDL) of the National Oceanic and Atmospheric Administration (NOAA) (Lenschow et al. 2000; Wulfmeyer and Janjić 2005; Lothon et al. 2009; Lenschow et al. 2012). Furthermore, horizontal wind profiles can be measured by VAD scans. A recent breakthrough in the development of compact, efficient, and eye-safe laser transmitters such as Er-doped fiber lasers permitted the development of very compact, all-solid-state systems, which are now commercially available from different companies (e.g., Philippov et al. 2004; Kameyama et al. 2007).

With respect to water vapor profiling, two methods are available: WVDIAL and WVRL. WVRLs measure profiles of water vapor mixing ratio m. As mixing ratio m can be readily converted to specific humidity q in the CBL by standard pressure and temperature profiles, in the following, we consider only q as the measured variable.

Operational WVRLs have been installed at only a few sites such as the ARM Program Southern Great Plains (SGP) WVRL (Turner et al. 2002). The design and installation of WVRL systems is usually the result of a special project. Extensive research led to a routine technique for the calibration of mixing ratio measurements, which is necessary for WVRL, with an accuracy of approximately 5% (Turner and Goldsmith 1999; Ferrare et al. 2006). Optimization of daytime performance, which is particularly critical for Raman lidar, was mainly achieved with the SGP Raman lidar and has not been accomplished at all sites. Typically, in the daytime, the noise error is less than $1\,\mathrm{g\,kg^{-1}}$ up to the CBL top using a combination of temporal and vertical resolutions of 10 s and 75 m, respectively. For the SGP WVRL, Wulfmeyer et al. (2010) and Turner et al. (2014a,b) demonstrated that this performance is sufficient for measuring profiles of higher-order moments of mixing ratio in the CBL. These higher-order moments derived from noisy lidar observations have also been validated with in situ measurements (Turner et al. 2014a). Furthermore, ARM has operated a nearly identical Raman lidar at Darwin, Australia, which provides a tropical dataset to complement the SGP midlatitude one.

The WVDIAL technique measures the absolute humidity ρ as a function of range. Similar to WVRL, it is straightforward to convert ρ in q with high accuracy by standard pressure and temperature profiles so that we continue to consider q as the measured variable. The technologically more demanding WVDIAL technique is less mature. To the best of our knowledge, just one ground-based system exists worldwide at the Institute of Physics and Meteorology (IPM) of the University of Hohenheim (UHOH) that has daytime turbulence resolution. Currently, this system has the highest temporal and spatial resolution of ground-based water vapor remote sensing systems (Behrendt et al. 2009; Wulfmeyer et al. 2015a). As DIAL does not need a calibration with respect to system constants, a very high accuracy of absolute humidity measurements is achieved. Recently, Späth et al. (2014) demonstrated by theoretical considerations and comparisons with soundings a systematic error of 2%. Because of the high signal-to-noise-ratio of the backscatter signals during daytime, the noise error is about an order of magnitude lower than WVRL using the same combination of vertical and temporal resolutions (Wulfmeyer et al. 2015a). Therefore, WVDIAL is an excellent instrument for measuring water vapor profiles, gradients, and higher-order moments (Muppa et al. 2015).

The TRRL technique is currently the only remote sensing technique that permits the profiling of temperature, its higher-order turbulent moments, and its gradient in the lower troposphere with high vertical resolution (Wulfmeyer et al. 2015a). Because of a recent breakthrough in system design and performance at IPM, Hammann et al. (2015) demonstrated that it is now possible to determine the strength of the inversion layer during daytime. Comparisons with soundings, which are necessary for the calibration of TRRL, revealed a systematic error of less than 1 K. The noise error of temperature profiles is less than 2 K using resolutions of 10 s and 100 m up to 2 km, which permitted the first profiling of higher-order moments of temperature (Behrendt et al. 2015). Noise error propagation [see Eq. (A14)] explains that it is still possible to extract accurate atmospheric variance measurements at this noise level and that these measurements are particularly significant in the EL. Therefore, the TRRL method is now suited to provide the temperature measurements necessary for the turbulence studies that are subject of this work. As it is easily possible to convert temperature profiles measured with TRRL into profiles of potential temperature and their fluctuations (Behrendt et al. 2011), we continue to use the variable θ in our considerations. Furthermore, the combination of WVRL, WVDIAL, and TTRL permits a straightforward interchange of the different humidity variables m, ρ, and q. Although none of these systems is commercially available yet, new technologies are emerging having this potential (e.g., Spuler et al. 2015).

A single lidar system does not measure fluxes directly. However, the combination of high-resolution vertical wind measurements by DL or a radar wind profiler with WVDIAL or WVRL and TRRL permits the determination of latent and sensible heat flux profiles with the eddy correlation (EC) technique directly, which was originally pioneered in Senff et al. (1994) and also demonstrated by Wulfmeyer (1999a) and Giez et al. (1999). The confirmation that sensible heat flux profiles can be measured by a DL–TRRL combination was recently provided by Wulfmeyer et al. (2015b).

Furthermore, the instantaneous CBL height $z_i(t)$ and correspondingly the mean z_i during the averaging period can be measured very accurately (e.g., Pal et al. 2010). Different methods using vertical gradients of mean profiles and variance profiles can also be compared. This is important for appropriate CBL scaling and for the localization of the EL.

c. *Proposed experimental design*

A considerable advantage of the application of the lidar system synergy in the CBL is its capability to profile atmospheric variables, their gradients, turbulent moments, and fluxes simultaneously. The combination of these lidar measurements permits a thorough study of

EL scaling by testing different combinations of the equations above allowing both the general relationships (e.g., is the water vapor variance proportional to the square of the mean gradient?) to be evaluated and estimates of the coefficients to be made.

For instance, the combination of lidar systems permits a complete verification of the set of Eqs. (9)–(11), Eqs. (16)–(18), and even Eqs. (20)–(22). If lidar systems demonstrate that these relationships are valid, their measurements can be used for deriving unique quantitative results with respect to fluxes and higher-order moments, as various constants can be determined by means of comparisons.

We recommend the following combination of lidar instruments:

- One scanning Doppler lidar for determining wind profiles in the CBL and the wind shear in the EL. This lidar would primarily perform VAD scans so that horizontal wind profiles could be derived.
- One vertically pointing Doppler lidar for vertical wind measurements and profiling of its higher-order moments. It may be possible to perform these measurements with a single Doppler lidar by switching between vertical and VAD operation modes, if the SNR is high enough. This would need to be investigated by studying the performance characteristics of the particular DL that would be used.
- One vertically pointing DIAL or WVRL with sufficient resolution measuring profiles of q and g as well as profiles of higher-order moments of q.
- One vertically pointing TRRL with sufficient resolution for measuring θ and γ profiles as well as higher-order moments of θ.

In addition to allowing the equations for fluxes and higher-order moments to be investigated, this combination permits a direct measurement of Ri as well as dissipation and molecular destruction rates.

d. *Strategy for investigation of CBL scaling based on lidar synergy*

Three important contributions of lidar measurements are possible: 1) the direct measurement and independent development of CBL similarity relationships based on the lidar synergy proposed above, 2) the test of the CBL relationships introduced in section 2b, and 3) use of these measurements for model verification. The direct determination of CBL similarity relationships is being addressed by field campaign data such as HOPE in spring 2013, SABLE in August 2014 in Germany, and at the ARM operational sites at SGP and Darwin, from which measurements of a combination of gradients and higher-order turbulent moments of atmospheric variables are available.

In this case, the following data analysis procedure is suggested:

1) Determination of all profiles of mean variables, their gradients, and higher-order moments and their characterization with respect to their errors, as discussed in sections 3c(1) and 3c(2).
2) Investigation of integral scales for making sure that the major part of the turbulent fluctuations is resolved.
3) Performance of the same procedure for the combined variables such as fluxes and dissipation and molecular destruction rates [sections 2b(1), 2b(2), and 3c(2)].

Using these results, the data can be combined and correlated in different ways in order to search for their relationships.

1) RICHARDSON NUMBER RELATIONSHIPS

For studying the relationships introduced in section 2b, first of all, it is essential to study the Ri_E dependence of variances and third-order moments. For instance, using Eqs. (16)–(18), we get

$$f_{w^2}(\mathrm{Ri}_E) = \frac{1}{C_{w^2}} \frac{\overline{w'^2}_E}{w_*^2}, \tag{59}$$

$$f_{\theta^2}(\mathrm{Ri}_E) = \frac{1}{C_{\theta^2}} \frac{\overline{\theta'^2}_E}{w_*^2(\gamma_E/N_E)^2}, \quad \text{and} \tag{60}$$

$$f_{q^2}(\mathrm{Ri}_E) = \frac{1}{C_{q^2}} \frac{\overline{q'^2}_E}{w_*^2(g_E/N_E)^2}. \tag{61}$$

For example, if the relationship for moisture [Eq. (19)] is valid, we find

$$\mathrm{Ri}_E = \frac{\dfrac{1}{C_{q^2}} \dfrac{\overline{q'^2}_E}{w_*^2(g_E/N_E)^2} - c_{q^2}}{1 - \dfrac{1}{C_{q^2}} \dfrac{\overline{q'^2}_E}{w_*^2(g_E/N_E)^2}}. \tag{62}$$

This equation makes a direct measurement of Ri_E possible merely based on a combination of temperature and water vapor lidar systems. This same approach allows for determining the values of the coefficients C_{q^2} and c_{q^2} as measurements of Ri_E will be available directly from the combination of DL and TRRL [Eq. (13)]. Naturally, many cases would be needed to develop uncertainty estimates for these coefficients and to see if these coefficients have any dependence on the meteorological regime. An analogous equation can be derived for Ri_E in dependence of temperature variance and gradients.

2) HIGHER-ORDER MOMENT RELATIONSHIPS

By the combination of gradient and variance measurements as well as the knowledge of Ri_E, Eqs. (16)–(18) can be studied. First attempts have already been performed by Wulfmeyer et al. (2010) and Turner et al. (2014b). However, for these studies neither wind nor temperature profiles were available yet, so further refinements and the use of more expanded datasets are necessary.

The question arises whether measurements of higher-order moments are helpful to get additional insight regarding turbulence in the EL. These lidar studies may lead to a refinement of the similarity relationships. For instance, focusing on humidity, if Eqs. (18) and (22) are valid, the skewness $\mathscr{S}_q$ in the EL should be negative because

$$\mathscr{S}_q := \frac{\overline{q'^3}_E}{(\overline{q'^2}_E)^{3/2}} \tag{63}$$

$$= \frac{C_{q^3} w_*^3 (g_E/N_E)^3 f_{q^3}(\mathrm{Ri})}{[C_{q^2} w_*^2 (g_E/N_E)^2 f_{q^2}(\mathrm{Ri})]^{3/2}} \tag{64}$$

$$= -\frac{C_{q^3}}{C_{q^2}^{3/2}} \frac{f_{q^3}(\mathrm{Ri})}{[f_{q^2}(\mathrm{Ri})]^{3/2}} \tag{65}$$

$$\cong -\frac{C_{q^3}}{C_{q^2}^{3/2}}, \tag{66}$$

where the last equation holds in the case of free convection. Under these conditions, the dependence on gradients is eliminated because the relationships are self-similar. Obviously, the similarity relationships propose a negative $\mathscr{S}_q$ in the EL. However, we already know from our measurements that this is not correct but $\mathscr{S}_q$ changes sign from negative to positive in the EL typically just below z_i (Wulfmeyer 1999a; Lenschow et al. 2000; Wulfmeyer et al. 2010; Turner et al. 2014b). The reason for this discrepancy is likely the inappropriate expansion of the scaling relationship for the variance [Eq. (18)] to the third-order moment [Eq. (22)]. This is a first interesting test of the similarity relationships demonstrating the potential of the lidar observations. Additionally, if the coefficients and the dependencies on Ri_E are known, Eq. (65) provides another estimate of Ri_E, which may be useful for studying the consistency of the set of equations.

For vertical wind, it is straightforward to see that the relationships prescribe that $\mathscr{S}_w > 0$. Indeed, this can be confirmed by most measurements (Lenschow et al. 2000, 2012). However, while $\mathscr{S}_w$ remains positive in the EL, there seems to be a negative slope leading to a reduction in the EL, which is not predicted. Thus, a very important topic will be the study of the behavior of third-order moments in the EL of the CBL.

3) FLUX RELATIONSHIPS

Particularly interesting is the application of EL scaling in a way that a minimum set of lidar systems can be applied for deriving fluxes taking advantage of their measurements of higher-order moments. There is indeed an interesting potential because, for example, the combination of Eq. (11) and the square root of Eq. (18) yields

$$Q_E = \frac{C_Q}{\sqrt{C_{q^2}}} w_* \sqrt{\overline{q'^2}_E} \frac{1 + c_Q/\mathrm{Ri}_E}{\sqrt{1 + c_{q^2}/\mathrm{Ri}_E}} \tag{67}$$

$$= \frac{0.025}{\sqrt{0.175}} w_* \sqrt{\overline{q'^2}_E} \frac{1 + 8/\mathrm{Ri}_E}{\sqrt{1 + c_{q^2}/\mathrm{Ri}_E}} \tag{68}$$

$$= 0.06 w_* \sqrt{\overline{q'^2}_E} \frac{1 + 8/\mathrm{Ri}_E}{\sqrt{1 + c_{q^2}/\mathrm{Ri}_E}} \tag{69}$$

$$\cong 0.06 w_* \sqrt{\overline{q'^2}_E}, \tag{70}$$

where the Eq. (70) holds in the case of free convection. In the case of significant wind shear, Eq. (67) and the studies of Ri_E in section 3d(1) or Eq. (62) can be combined so that it may be possible to use a WVDIAL and a TRRL for the direct determination of entrainment moisture fluxes.

Another possibility is to relate the flux with variance and gradients by eliminating w_*:

$$Q_E = -\frac{C_Q}{C_{q^2}} \frac{N_E}{g_E} \overline{q'^2}_E \frac{1 + c_Q/\mathrm{Ri}_E}{1 + c_{q^2}/\mathrm{Ri}_E} \sqrt{1 + \frac{1}{\mathrm{Ri}_E}}, \tag{71}$$

$$Q_E \simeq -\frac{C_Q}{C_{q^2}} \frac{N_E}{g_E} \overline{q'^2}_E \sqrt{1 + \frac{1}{\mathrm{Ri}_E}}, \quad \text{and} \tag{72}$$

$$Q_E \approx -\frac{C_Q}{C_{q^2}} \frac{N_E}{g_E} \overline{q'^2}_E \simeq -0.14 \frac{N_E}{g_E} \overline{q'^2}_E, \tag{73}$$

again where the last equation is proposed to be valid in the free convection limit. Comparing Eqs. (71)–(73) with the surface latent heat flux, it can be determined whether the CBL is drying or moistening, as long as moisture advection can be neglected. Obviously, the CBL is moistening if the ratio $V = Q_E/Q_0 < 1$, which translates to

$$V = \frac{Q_E}{Q_0} = 0.06 \frac{w_* \sqrt{\overline{q'^2}_E}}{Q_0} \frac{1 + 8/\mathrm{Ri}_E}{\sqrt{1 + c_{q^2}/\mathrm{Ri}_E}} \tag{74}$$

$$= 0.06 \frac{\sqrt{\overline{q'^2}_E}}{q_*} \frac{1 + 8/\mathrm{Ri}_E}{\sqrt{1 + c_{q^2}/\mathrm{Ri}_E}} \tag{75}$$

$$\cong 0.06 \frac{\sqrt{\overline{q'^2}_E}}{q_*}, \tag{76}$$

with the last equation holding in the case of free convection.

Of course, if the relationships for Q_E are verified, they can also be used for determining the flux divergence in the CBL, which is extremely important for CBL TP. Assuming a linear flux profile, the flux divergence is simply

$$\frac{\partial}{\partial z}\overline{w'q'} = \frac{Q_E - Q_0}{z_i} \tag{77}$$

$$\simeq \frac{0.06\sqrt{\overline{q'^2}_E}w_* - Q_0}{z_i}. \tag{78}$$

Obviously, a couple of comprehensive relationships can be derived, which are worth an extensive evaluation.

In an additional step, it is also possible to investigate the closure of the budget equations for mean variables, as demonstrated in Senff et al. (1994), Wulfmeyer (1999a,b), as well as for higher-order moments and fluxes.

4) Dissipation and molecular destruction rates

The lidar measurements allow the profiling of the integral scales throughout the CBL including the EL. If the major part of the turbulent fluctuations is resolved, the parameters of the structure function can be determined. Therefore, we are proposing here a new technique for the combination DL, TRRL, and WVDIAL or WVRL in order to determine TKE dissipation rates as well as the destruction rates of temperature and humidity variances based on Eqs. (43)–(45), Eqs. (47) and (48), Eq. (52) and (53), and Eqs. (56) and (57).

4. First results using WVDIAL and TRRL

a. Dataset

We present data collected during intensive observations period (IOP) 5 of HOPE, which was performed in spring 2013 close to the city of Jülich, Germany. IOP5 was executed on 20 April 2013. We focus on a dataset collected with the IPM WVDIAL and the TRRL between 1130 and 1230 UTC. The lidar systems were located at site close to the village of Hambach near Research Centre Jülich at 50°53′50.56″N, 6°27′50.39″E and 110 m above sea level.

During IOP5, the HOPE domain was under the influence of a high pressure system over the Baltic Sea and a cold front over the Alps to the southeast. The local conditions were measured by a weather and energy balance closure station a few meters from the site. The surface pressure at the measurement site was $p_0 \simeq 1020$ hPa. The horizontal wind speed at 5-m height was $1.5\,\mathrm{m\,s^{-1}}$ from northeast turning to eastern directions at the CBL top, as revealed by a radio sounding launched at the measurement site at 1300 UTC. The surface temperature was low with 284 K. Because of the large-scale conditions, rather dry air was advected into the region resulting in a surface specific humidity of merely $3.4\,\mathrm{g\,kg^{-1}}$ corresponding to a relative humidity (rh) of approximately 43%. Further details concerning the meteorological conditions are found in Muppa et al. (2015).

Except for a few cirrus clouds, the atmosphere was cloud free and contained only a few aerosol layers in the free troposphere. The surface heating was significant resulting in sensible heat flux of $247\,\mathrm{W\,m^{-2}}$, whereas the evapotranspiration was modest with $89\,\mathrm{W\,m^{-2}}$. The friction velocity was $u_* \simeq 0.7\,\mathrm{m\,s^{-1}}$, corresponding to a Monin–Obukhov length of $L \simeq -126$ m.

b. Results derived by lidar synergy

We are focusing on the synergy of the IPM WVDIAL and the TTRL systems. Doppler lidar data had to be excluded because the vertical velocity variance and skewness, as well as the horizontal winds, have not been processed in detail yet. Therefore, a full analysis of fluxes and variances, and their relationships with gradients and dependences on Ri_E, is not possible. In any event, a full exploitation of all equations presented in sections 2 and 3 is beyond the scope of this work and subject of future activities.

However, even without the knowledge of Ri_E, a large number of relations could be studied for the first time here. This is due to the fact that the WVDIAL and TRRL measurements are providing mean profiles and their vertical gradients of specific humidity and potential temperature, variance profiles, and insight into structure coefficients in the same vertical air column, simultaneously. For this study, both the WVDIAL and the TRRL data were processed with a temporal resolution of 10 s and vertical resolutions of 100 m allowing for a consistent analysis of gradients and turbulent moments. Additionally, the TTRL data were corrected with respect to systematic errors induced by incomplete overlap between laser transmitter and field of view of the telescope up to 800 m with a time-independent correction function (Hammann et al. 2015). Afterward, the WVDIAL absolute humidity measurements and the TRRL temperature measurements were transformed into specific humidity and potential temperature using a hydrostatic pressure profile.

The mean specific humidity, potential temperature, and relative humidity profiles and their gradients during the measurement period are presented in Fig. 3 (top). The system noise errors and the estimate of the mean CBL depth z_i are also indicated. As mentioned above, the specific humidity in the ML was rather low with

$3\,\mathrm{g\,kg^{-1}}$. Toward the entrainment layer already a strong decrease of the specific humidity was observed decreasing further to $0.1\,\mathrm{g\,kg^{-1}}$ in the lower free troposphere. This resulted in a strong reduction of rh around the EL as well. The potential temperature profile shown in Fig. 3 shows a well-mixed CBL (as also confirmed by soundings) up to 1000 m with a mean $\theta \simeq 282.5$ K. The moisture decrease above and the large vertical extent of the region with increasing potential temperature likely indicates an entrainment drying CBL.

During the time period of interest, the CBL was well developed and reached a quasi-stationary depth, as confirmed by the lidar backscatter profiles (not shown). Whereas many different definitions of z_i are available (e.g., Cohn and Angevine 2000; Pal et al. 2010) and some uncertainties remain, we could take advantage of the synergy of our measurements. For this purpose, we evaluated the gradients of the lidar backscatter signals, the minimum of the mean water vapor gradient, and the maximum of the potential temperature gradient in the EL as well as the locations of the maxima of the variance profiles. This resulted in $z_i \approx 1280$ m with a standard deviation of 60 m derived from the instantaneous $z_i(t)$ values of the backscatter gradients. The latter value multiplied by 2 can be considered as an estimate of the mean EL thickness and resulted in $\Delta_{\mathrm{EL}} \simeq 120$ m. This result of z_i was consistent within 20 m with the radio sounding launched at 1300 UTC.

Using the estimate of z_i, we derived a vertical velocity scale of $w_* \simeq 2\,\mathrm{m\,s^{-1}}$, a convective time scale of $t_* \simeq 10.7$ min, a humidity scale of $q_* \simeq 0.015\,\mathrm{g\,kg^{-1}}$, and a potential temperature scale of $\theta_* \simeq 0.1$ K. Furthermore, we estimated the corresponding temperature gradient by taking the range $z_i - \Delta_{\mathrm{EL}}/2$, $z_i + \Delta_{\mathrm{EL}}/2$, which yielded $\gamma_E \simeq 0.02\,\mathrm{K\,m^{-1}}$ or a temperature jump of approximately 2 K in the EL. This resulted in a Brunt–Vaisala frequency of $N_E \simeq 0.026$ Hz and a local Richardson number $\mathrm{Ri}_l = \Delta\theta/\theta_* \simeq 20$. As shown in Fig. 3, the minimum specific humidity gradient in the EL was approximately $-0.012\,\mathrm{g\,kg^{-1}\,m^{-1}}$ and the averaged gradient in the EL yielded $g_E \simeq -0.01\,\mathrm{g\,kg^{-1}\,m^{-1}}$.

By means of the analyses described in section b of the appendix (see also Lenschow et al. 2000; Wulfmeyer et al. 2010), we derived profiles of the integral scales, variances, and third-order moments of potential temperature and specific humidity. In all these figures, black error bars indicate noise errors and the colored error bars the sampling errors.

Figure 4 presents the profiles of the integral scales $\mathscr{T}_\theta$ (top panel) and $\mathscr{T}_q$ (bottom panel). In these panels, we also compared their determination by a numerical integration from lag 0 to the first zero crossing of the autocovariance function with the theoretical result given in Eq. (42). The outliers in the numerical integration are due to systematic errors, if very low variance levels are determined by the extrapolation of the autocovariance function, as in the numerical integration the autocorrelation function must be used [see Eq. (41) and Fig. A1]. We recommend the use of Eq. (42) because it gives more robust results at low variance levels and compares very well with the numerical integration otherwise.

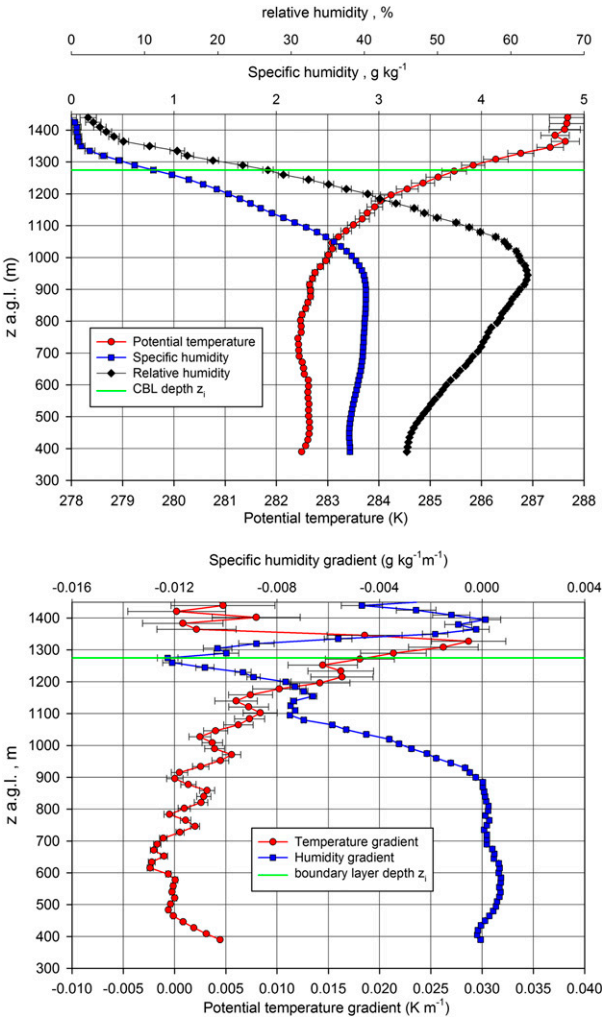

FIG. 3. (top) Mean profiles of specific humidity and potential temperature during IOP5 (1130–1230 UTC). (bottom) Corresponding vertical gradient profiles. The error bars due to system noise and the estimate of z_i are also indicated.

For potential temperature, a rather constant profile in the CBL was determined with $\mathscr{T}_\theta \simeq 50$ s. In contrast, $\mathscr{T}_q$ showed a reduction from the ML to the EL from approximately 150 to 50 s. In both profiles, fine structures appear, which are not fully understood yet. Currently, we suppose that these are due to sampling statistics. These results also confirm that the resolution of the lidar profiles was high enough to resolve the temperature and

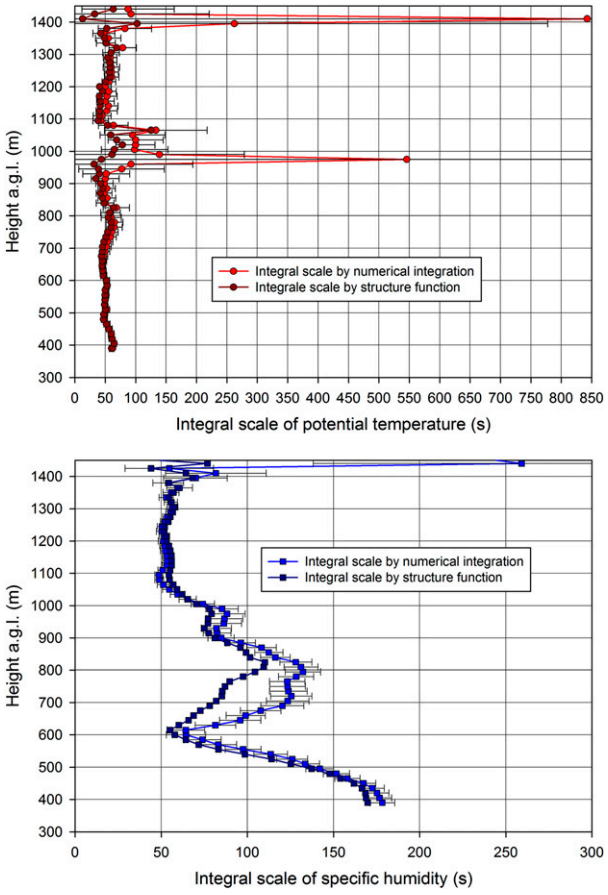

FIG. 4. (top) Potential temperature integral scale derived using the integration of the autocovariance function to the first zero crossing or using the new Eq. (42). (bottom) As in (top), but for specific humidity.

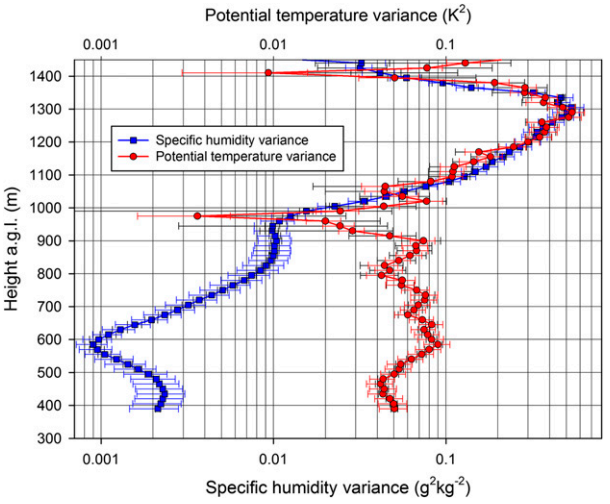

FIG. 5. The specific humidity and potential temperature variance profiles. The error bars in the same color as the plots are the sampling errors and the black error bars are the noise errors.

humidity fluctuations into the inertial subrange even in the EL.

The potential temperature and specific humidity variance profiles are depicted in Fig. 5. To demonstrate the high SNR of the measurements, the profiles are plotted on a logarithmic scale. Again, some fine structures in the profiles are found, which may be due to sampling statistics or a too-strong noise correction at low variance level. Otherwise, the potential temperature variance profiles show a nearly constant variance of $0.07\,\mathrm{K}^2$ in the ML and the expected peak in the EL with an amount of $0.5\,\mathrm{K}^2$. In contrast, the specific humidity variance profile is generally increasing from very low levels by an order of magnitude to $0.1\,\mathrm{g}^2\,\mathrm{kg}^{-2}$ in the ML. In the EL, the typical peak is reached with a value of $0.5\,\mathrm{g}^2\,\mathrm{kg}^{-2}$. It is likely a coincidence in this case that the absolute values of potential temperature and specific humidity variances in the EL are similar.

Profiles of the third-order moments are presented in Fig. 6. In the ML, both profiles indicate a symmetric distribution of the fluctuations. However, in the EL, below z_i the third-order moment turns positive for the potential temperature and negative for the specific humidity fluctuations. Close to z_i, the moments show a zero crossing and are changing sign above, which is clearly visible in the specific humidity but less pronounced in potential temperature, however, likely as a result of a larger noise level in the latter.

c. *Discussion*

The results presented in Figs. 3–6 can be used to evaluate several relationships proposed in this work. The necessity to derive improved relationships for exchange and turbulent processes in the EL becomes already evident by noting that the standard potential temperature and specific humidity scales derived in section 4b cannot explain the observed variances in this layer.

The main weakness in our study is the lack of knowledge of Ri_E. However, the local $\mathrm{Ri}_l \simeq 20$ and the lack of strong shear in the radiosonde data indicate that the case was not too far from the free-convection limit. Therefore, in the following, we disregard any Ri_E dependencies. Furthermore, we assume that w_* is a reasonable scaling variance for the vertical wind fluctuations even in the EL.

Considering these uncertainties, we start with an evaluation of the variances in the EL. Using Eqs. (17) and (18) and the proposed coefficients C_{θ^2} and C_{q^2}, we get estimates of $\overline{\theta'^2} \approx 0.1\,\mathrm{K}^2$ and $\overline{q'^2} \approx 0.1\,\mathrm{g}^2\,\mathrm{kg}^{-2}$. Thus, we achieved an underestimation of the variances in the EL by a factor of 5. Obviously, at least one of the assumptions, the validity of the free convection limit, the scaling with w_*, or the values of the constants derived by LES were not valid.

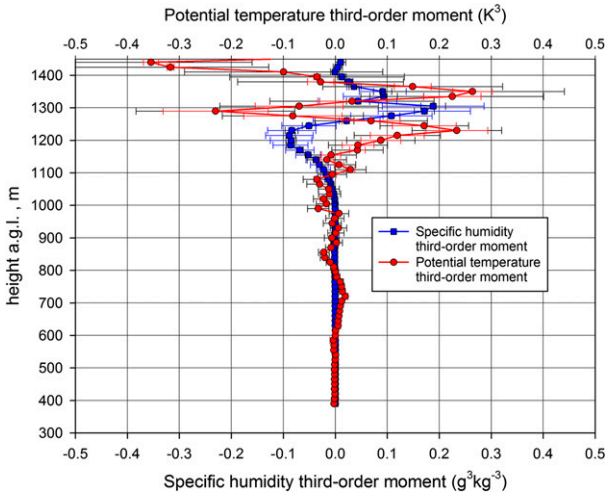

FIG. 6. The specific humidity and potential temperature third-order-moment profiles. The same convention for the colors and error bars is used as in Fig. 5.

We also tested Eqs. (70) and (73) for the water vapor entrainment flux Q_E. Using Eq. (70) we achieved $Q_E \approx 210\,\mathrm{W\,m^{-2}}$ and using Eq. (73) we got $Q_E \approx 450\,\mathrm{W\,m^{-2}}$. In both cases, an entrainment drying CBL was confirmed [see also Eq. (76)]. However, because of the strong drying at the CBL top (see Fig. 3), the latter value was likely closer to reality. This indicates that we may have to go away from the scaling using w_* in the EL and it is better to use potential temperature and specific humidity gradients.

Using Fig. 6, we can evaluate also the scaling proposed in Eqs. (21), (22), and (66). It turns out that the gradient scaling does not work in the case of third-order moments because the third-order moment changes sign in the EL leading to a complex structure of the profiles. With respect to water vapor, this structure was also found in other lidar measurements (Wulfmeyer 1999b; Wulfmeyer et al. 2010; Turner et al. 2014b) so that this seems to be common in the CBL. With respect to temperature, we are confirming this complex structure for the second time using active remote sensing—the first time it was shown using TRRL measurement by Behrendt et al. (2015) albeit with different values of the negative and positive maxima. Couvreux et al. (2007) detected and analyzed this structure by LES. They argued that this behavior is due to the deformation of eddies in the region of the inversion causing different updraft and recoiling structures. In the future, further insight in and quantification of the behavior of third-order moments should be collected by additional observations and dedicated LES and DNS runs by analyzing the third-order moment budgets.

The use of Eq. (39) in combination with Eq. (A9) also allowed us to get some insight in the profiles of the structure function coefficients k_q and k_θ. Figure 7 presents the results. In the top panel, except at very low variance levels, we found a striking linear relationship between these coefficients and the corresponding variances with a very similar slope for specific humidity and potential temperature. By a linear fit, we found $\overline{q'^2} \simeq 26.5\,\mathrm{s}^{2/3} k_q$ and $\overline{\theta'^2} \simeq 26.2\,\mathrm{s}^{2/3} k_\theta$. Furthermore, we studied the ratio k_q/k_θ between these coefficients, which corresponds to the ratio of the molecular destruction rates of humidity and temperature variances. The results are presented in the bottom panel of Fig. 7. Except some outliers due to low SNR and taking a ratio of noisy signals, in the ML, the destruction rate is much smaller for humidity than for temperature. However, in the EL, the ratio reaches approximately the same value of 1 so that the destruction rates are becoming similar.

Despite some missing information, we demonstrated first results comparing profiles of gradients, variances, and the coefficient of the structure function from the ML through the EL in a quasi-stationary CBL. Whereas the variances in the EL were underestimated by the gradient function relationships in comparison to the measurements, reasonable results were achieved for the water vapor entrainment flux. The structure of the third-order moments in the EL is more complex than can be described by gradient relationships. Interesting results were found with respect to the behavior of the structure function coefficients showing a different ratio of molecular destruction rates in the ML and the EL. In the future, it is essential that these studies are extended by simultaneous measurements of wind profiles and vertical velocity statistics because the dependence of the relationships on the functions $f(\mathrm{Ri}_E)$ for variances and fluxes as well as the validity of scaling with the convective velocity scale have to be investigated. For this purpose, continuous measurements of the daily cycle of the CBL during field campaigns and/or observatories with sufficient equipment of lidar systems are necessary. Furthermore, the dependence of the results on the resolution of the lidar systems and of dedicated LES runs needs be explored.

5. Summary and outlook

In this work, we presented methodologies for improving the representation of turbulent transport processes and entrainment in weather and climate models for advanced simulations of water and energy cycles. Usually, turbulent transport processes are represented by the turbulence parameterization (TP), as long as the model grid increment is approximately 1 km or more.

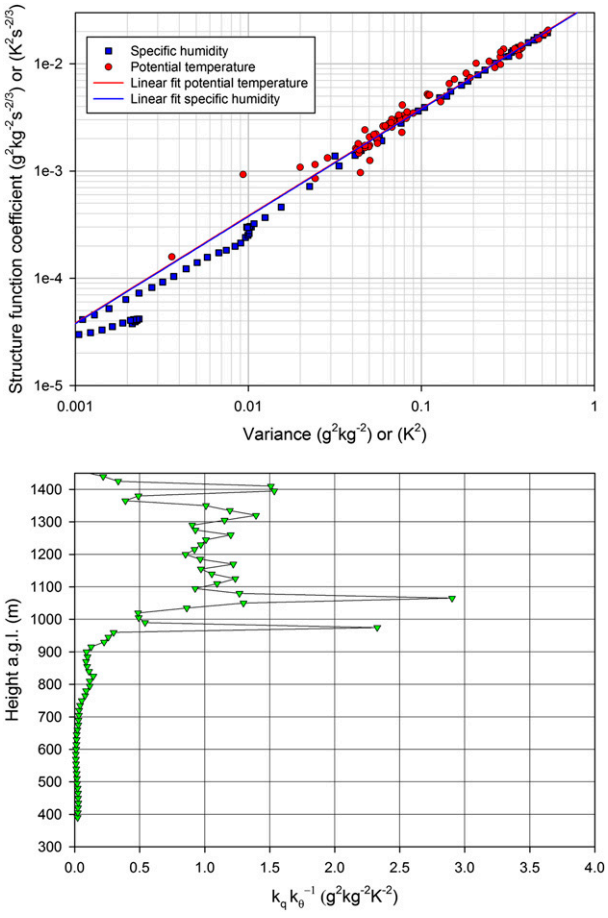

FIG. 7. (top) Relation between variances and structure function coefficients for potential temperature and specific humidity. Additionally, the results of a linear fit are shown. (bottom) The ratio between the coefficient in dependence of height.

However, it is controversial at what grid increment the turbulence should be explicitly simulated without any TP so that the model is running in the large-eddy simulation (LES) mode. Because over many regions of Earth, convection initiation in the daytime is critical for the formation of clouds and precipitation, we are focusing on the investigation of turbulence in the daytime atmospheric convective boundary layer (CBL) with low cloud coverage.

Studies of turbulent transport processes and entrainment can be performed either by LES or high-resolution observations. LES has been used for the investigation of turbulence for a long time, and many aspects of TPs have been derived from the corresponding results. However, it should not be forgotten that a detailed simulation of land surface–atmosphere exchange and feedback requires a realistic representation of the heterogeneity of the land surface with respect to soil properties, land cover, and orography. Furthermore, it is fundamental to include the simulation of gravity waves at the CBL top, as these are contributing to the strength of entrainment. Only a few LES studies—if any—have been performed that fulfill these requirements. Therefore, strong efforts are still needed to improve LES by imbedding the simulations in a realistic large-scale environment. The latter is leading to the so-called gray-zone experiments where a chain of models resolving down to the LES scale can be compared with respect to their performance in a realistic synoptic setting. In any case, model simulations either in the form of gray-zone experiments or more idealistic LES must be verified with respect to their performance. Furthermore, any TPs require physically based relationships concerning entrainment processes, which must be verified by observations.

We present a new approach for the understanding and simulation of entrainment in the EL at the top of the CBL. After a discussion of the vertical structure of the CBL, EL scaling variables are introduced, which can be combined to derive a series of equations for determining variances and fluxes. These are related to gradients of wind, temperature, and humidity in the EL. It is also shown that the vertical exchange through the EL should contain a functional dependence of the gradient Richardson number Ri_E. Suggestions for these relationships are made. Furthermore, the autocovariance functions of the variables are considered, which can be modeled in the inertial subrange with the structure function for stationary and homogeneous turbulent processes. Physical relationships between the integral temporal and spatial scales and the turbulent quantities are derived, which can be tested by observations. New equations are introduced for profiling the TKE dissipation rate as well as the molecular destruction rates of humidity and temperature variances.

The verification of the relationships requires the measurements of wind, temperature, and humidity profiles as well as their gradients in the CBL including the EL. It is necessary that the corresponding instruments resolve their fluctuations for determining profiles of higher-order moments and of fluxes simultaneously.

We demonstrate that these verification efforts can be realized by a new synergy of DL for profiling the vertical and horizontal wind, WVDIAL or WVRL for humidity profiling, and TRRL for temperature profiling. This combination of instruments is essential but also sufficient for a complete analysis of the similarity relationships. A thorough analysis of the new generation of WVRL, WVDIAL, and TRRL lidar systems, where the last two of them have been developed at the IPM of the UHOH, demonstrates that these systems are capable of fulfilling the measurement needs. A detailed analysis of systematic and noise errors of mean profiles, their

gradients, higher-order moments, fluxes, and dissipation and molecular destruction rates is presented, which can be used to confirm the sufficient performance of these lidar systems.

A straightforward strategy of using the data from these lidar systems is developed. After all profiles of interest are determined and their error bars are characterized, the results can be combined in different ways. For instance, the data can be used for determining Ri_E to study the functional dependence of Ri_E influencing variance and flux profiles. A series of equations is derived to investigate variance- and third-order moment–gradient relationships, flux–variance relationships, and flux–gradient relationships.

We demonstrate that the DL–WVDIAL/WVRL–TRRL synergy has at least three functions: 1) a complete set of equations can be tested for deriving variances and fluxes by gradient relationships; 2) LES can be verified in great detail by studying profiles of second-, third-, and fourth-order moments; and 3) new relationships for fluxes and variances can be derived forming the basis for budget analyses and new TPs.

First tests of these relationships were presented using a dataset from HOPE. Simultaneous measurements of mean profiles and gradients of potential temperature as well as specific humidity and their variances are shown and analyzed. We showed that the similarity relationships underestimate the measured variance, if the free-convection limit was present and the constants previously derived by LES are valid. Furthermore, we assumed that the convective velocity scale is an appropriate scaling variable. The application of a gradient–variance similarity relationship for the entrainment water vapor flux gave reasonable results and indicated an entrainment-drying CBL during the measurement period. The variances were proportional to the fit coefficients of the structure function and the molecular destruction rates of potential temperature and specific humidity variances became similar in the EL. In the future, measurements of additional scaling variables using DL have to be added to refine these studies.

So far, this combination of measurements has only been realized during the HOPE and SABLE field campaigns. Further datasets are available from observatories such as the ARM SGP and Darwin sites but may require some redesign and improvement of instrument equipment and performance there. We propose to perform dedicated field campaigns for studying the proposed relationships and to extend current observatories to fulfill the required measurement needs. Ideally, the operation of this basic synergy of active instruments should be supported by airborne in situ as well as passive and active remote sensing measurements using a combination of lidar and radar systems extending the measurements in clouds. These efforts should be accompanied by gray-zone simulations down to the LES or even the DNS scale. The relationships and equations in this work as well as simulations of the same scales will enable us to reach a new level of detail and accuracy for testing and developing advanced TPs in the CBL.

Acknowledgments. This work was supported by the Cooperative Institute for Environmental Studies (CIRES) in Boulder, Colorado, by a Visiting Fellow Award for the first author. Furthermore, this study was performed within the German Science Foundation (DFG) Research Unit FOR1695 "Regional Climate Change" and the Federal Ministry of Education and Research (BMBF) program High Definition Clouds and Precipitation (HD(CP)^2). This research was also supported by the National Severe Storms Laboratory (NSSL) in Norman, Oklahoma, and the U.S. Department of Energy (DOE) Atmospheric System Research (ASR) via Grant DE-SC0006898.

APPENDIX

Error Analysis of Lidar Profiles

a. Systematic errors

For all lidar systems introduced above, stable system performance has been demonstrated so that any systematic errors should be constant in time during turbulence measurements. The corresponding errors of wind, humidity, and temperature profiles can be taken from the specifications summarized in section 3b. As the height dependence of these errors is very low as well, their effect on gradients can be neglected. It is interesting to investigate the effect of systematic errors on turbulent quantities as well. If the systematic error is just a constant offset, it does not have an influence on the fluctuations so that this effect can be neglected. However, in many lidar systems and other calibrated observing systems, systematic deviations from the mean can be caused by errors in a calibration constant. In this case, the error of the fluctuations can be analyzed as follows using q as an example. If q_T and q_M are the true and the measured values then

$$q_T(t) = q_M(t) + Fq_M(t), \tag{A1}$$

where F is the relative systematic error of the measurement of q_M. Then

$$q'_T(t) = q_T(t) - \overline{q}_T \quad \text{and} \tag{A2}$$

$$q'_M(t) = q_M(t) - \overline{q}_M. \tag{A3}$$

Thus, the systematic error $\Delta q'_M$ in the measurement of the fluctuations of q reads

$$\Delta q'_M(t) = q'_T(t) - q'_M(t) = q_T(t) - \overline{q}_T - [q_M(t) - \overline{q}_M]. \quad \text{(A4)}$$

Using Eq. (A1), it follows

$$\Delta q'_M(t) = q_M(t) + Fq_M(t) - \overline{q}_M - F\overline{q}_M - q_M(t) + \overline{q}_M \quad \text{(A5)}$$

$$= Fq_M(t) - F\overline{q}_M = F[q_M(t) - \overline{q}_M] \quad \text{(A6)}$$

$$= Fq'_M(t). \quad \text{(A7)}$$

Applying Eq. (A7) to the derivation of variances, we get

$$\overline{q'^2}_M = (1+F)^2\overline{q'^2}_T \simeq (1+2F)\overline{q'^2}_T, \quad \text{(A8)}$$

where $\overline{q'^2}_M$ is the variance measured including the systematic effect by F, for example, by an inaccurate calibration. Basically, the systematic error doubles, if variances are considered. As F is constant in time and just a few percent for all lidar systems (DL, WVDIAL, WVRL, and TRRL) considered here, systematic errors in the measurements of fluctuations can be neglected.

b. Sampling and noise errors

Error bars due to sampling and noise statistics have to be derived and considered for all profiles in order to specify the significance of the results. Sampling errors are critical for ground-based measurements owing to the considerable integration time to collect turbulent fluctuations with high statistical certainty. Sampling errors can be reduced by performing many measurements under similar meteorological conditions or by the design and operation of ground-based networks. Sampling errors were derived for all kinds of turbulent profiles and specified in Lenschow et al. (1994, 2000); therefore, they are not repeated here.

For all lidar-derived profiles, noise error bars have also to be specified, as their propagation into turbulence profiles is still significant. It is the strength of the lidar technique that these error bars can be derived for each turbulence profile under the current meteorological conditions without any additional assumptions. A very convenient and robust technique for determining noise error profiles was introduced in Lenschow et al. (2000) and applied there to DL and WVDIAL measurements. Wulfmeyer et al. (2010) extended this technique to WVRL and Behrendt et al. (2015) to TRRL turbulence measurements.

This technique is based on the extrapolations of the measured autocovariance functions to lag 0 by the structure functions given in Eqs. (35)–(37). We assume

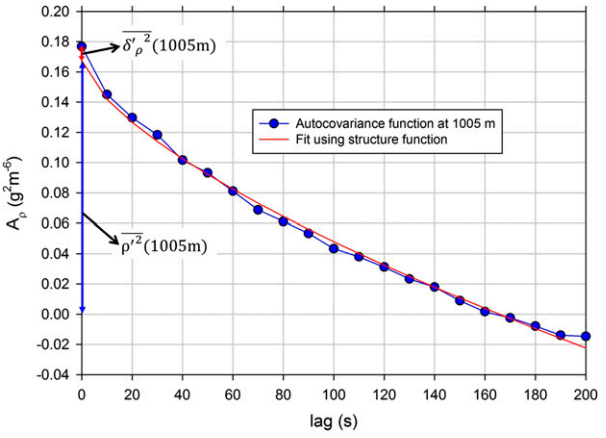

FIG. A1. Separation of atmospheric and noise variance by the fit of the structure function to the autocovariance function A_ρ for absolute humidity measured with the IPM WVDIAL.

that the noise errors between different lags are uncorrelated, which is the case for all lidar systems of interest here. It follows, for example, for specific or absolute humidity ρ measurements at lag 0:

$$A_q(0) = \overline{q'^2} + \delta^2 \quad \text{or} \quad A_\rho(0) = \overline{\rho'^2} + \delta_\rho^2, \quad \text{(A9)}$$

where δ^2 and δ_ρ^2 are the specific or absolute humidity system noise variances at the corresponding temporal and range resolutions. Figure A1 demonstrates this technique for a WVDIAL absolute humidity measurement performed during the SABLE campaign at 1100–1200 UTC 21 August 2014 at a height of 1005 m using a temporal resolution of 10 s. Clearly the noise and the atmospheric variances can be separated. The turbulence is well resolved, as observed by the good fit to the structure function, and the noise contribution is very small. The fit results in $\overline{\rho'^2} \simeq 0.17\,\mathrm{g^2\,m^{-6}}$ and a noise variance of $\delta_\rho^2 \simeq 0.01\,\mathrm{g^2\,m^{-6}}$, which corresponds to a noise error standard deviation of just $\delta_\rho \simeq 0.1\,\mathrm{g\,m^{-3}}$.

Extended studies of this technique (e.g., Turner et al. 2014b) demonstrated that this separation is routinely possible at all height levels, at much higher noise levels, and even in the presence of clouds. As it was not explicitly mentioned in Lenschow et al. (2000), we are deriving here the error propagation for noise errors of gradients of humidity and temperature profiles as well as for errors of third- and forth-order moments of atmospheric variables. Noise errors of fluxes as well as dissipation and molecular destruction rates are also considered.

1) GRADIENTS

Gradients of humidity and temperature are derived from absolute humidity or mixing ratio profiles (WVDIAL or WVRL) or from temperature profiles (TRRL). In contrast

to radio soundings, the representativeness is improved by continuous measurements of profiles of the variable of interest with a temporal resolution of 1–10 s and averaging them over time periods of 30–120 min, typically. The gradient, for example, for humidity, can be approximated by calculating the differential quotient

$$g(\overline{z}) = \frac{q(z+\Delta z) - q(z)}{\Delta z}, \tag{A10}$$

where Δz is the range resolution of the lidar measurement and the gradient is located at $\overline{z}$, the mean value between z and $z + \Delta z$. After determination of the noise variance δ^2 at each vertical bin of humidity profile, the error σ_g of the gradient reads

$$\sigma_g \simeq \sqrt{\frac{\delta^2}{N}}\,\frac{\sqrt{2}}{\Delta z}, \tag{A11}$$

considering that the noise errors at the range bins $z + \Delta z$ and z are nearly the same and statistically independent. Here, N is the number of samples during the averaging time for the determination of the gradient and turbulent quantities.

2) HIGHER-ORDER MOMENTS

Using the error propagation for the fluctuation q' of water vapor, higher-order moment profiles can be characterized with respect to noise errors. For instance, for the noise error $\sigma_{q'^2}$ of the variance we consider that noise errors are independent in each sample q'_i of the fluctuations and achieve by error propagation

$$\sigma^2_{q'^2} \simeq \frac{1}{N^2}\sum_i \left[\frac{\partial}{\partial q'_i}(q'_i)^2\right]^2 \delta_i^2 \simeq \frac{4}{N^2}\sum_i (q'_i)^2\delta_i^2 \simeq \frac{4}{N}\overline{q'^2}\delta^2. \tag{A12}$$

Thus,

$$\sigma_{q'^2} \simeq 2\sqrt{\overline{q'^2}}\sqrt{\frac{\delta^2}{N}} \quad \text{and} \tag{A13}$$

$$\sigma_{q'^2} \simeq 2\overline{q'^2}\sqrt{\frac{\delta^2}{\overline{q'^2}N}}. \tag{A14}$$

Applying these equations to the example from Fig. A1, which used a time resolution of 10 s and an averaging time of 1 h ($N = 360$), we get an absolute error of $\sigma_{q'^2} \simeq 0.004\,\mathrm{g^2\,m^{-6}}$ and a relative error of $\sigma_{q'^2}/\overline{q'^2} \simeq 3\%$, which is quite acceptable and demonstrates the low noise of the IPM WVDIAL.

Applying the same principle of Eq. (A12) to higher-order moments, we get for the noise error $\sigma_{q'^3}$ of the third-order moment

$$\sigma_{q'^3} \simeq 3\sqrt{\overline{q'^4}\frac{\delta^2}{N}} \simeq 3\sqrt{3\overline{q'^2}}\sqrt{\frac{\delta^2}{N}}. \tag{A15}$$

We applied the Isserlis theorem to the fourth-order moment as $\overline{q'^4} \simeq 3\overline{q'^2}^2$ assuming that higher-order moments do not deviate too much from a Gaussian distribution.

Then, Eq. (A15) can also be written in the following forms:

$$\sigma_{q'^3} \simeq \frac{3}{2}\sqrt{3}\sqrt{\overline{q'^2}}\sigma_{q'^2} \tag{A16}$$

or

$$\frac{\sigma_{q'^3}}{\overline{q'^3}} \simeq 3\sqrt{3}\,\frac{1}{\mathscr{S}_q}\sqrt{\frac{\delta^2}{\overline{q'^2}N}} \tag{A17}$$

by introducing the skewness $\mathscr{S}_q$ of the time series.

The noise error of the fourth-order moment is calculated accordingly and we derive

$$\sigma_{q'^4} \simeq 4\sqrt{\overline{q'^6}}\sqrt{\frac{\delta^2}{N}} \simeq 4\sqrt{15\overline{q'^2}^3}\sqrt{\frac{\delta^2}{N}} \tag{A18}$$

again using an Isserlis theorem but here for $\overline{q'^6} \simeq 15\overline{q'^2}^3$. Analogous to the third-order moment we get the following relationships:

$$\sigma_{q'^4} \simeq \frac{\sqrt{15}}{2}\overline{q'^2}\sigma_{q'^2} \tag{A19}$$

or

$$\frac{\sigma_{q'^4}}{\overline{q'^4}} \simeq 4\sqrt{15}\,\frac{1}{\mathscr{K}}\sqrt{\frac{\delta^2}{\overline{q'^2}N}} \tag{A20}$$

with the kurtosis $\mathscr{K}$ of the time series. Obviously, the noise errors of the nth moment scale approximately with

$$\sigma_{q'^n} \propto \sqrt{\overline{q'^2}}^{(n-2)}\sigma_{q'^2} \quad \text{for} \quad n \in \mathbb{N} \geq 2. \tag{A21}$$

Using these relationships, a full error propagation is possible for all vertical profiles of higher-order moments and their vertical gradients so that errors can be derived for all variables presented in the equations above. The errors scale with the standard deviation of noise during the averaging time. Consequently, as long as no nonlinearities occur in the derivation of fluctuations, it is better to maximize the time resolution so that the atmospheric variability is resolved as far as possible into the inertial subrange. Furthermore, the noise errors of the turbulent moments scale with powers of

atmospheric variances so that the noise errors remain small in the EL.

3) FLUXES

It is also important to study noise errors in fluxes. Here, we achieve

$$\sigma_{w'q'} \simeq \sqrt{\overline{q'^2}\frac{\delta_w^2}{N} + \overline{w'^2}\frac{\delta_q^2}{N}} \tag{A22}$$

$$\simeq \sqrt{\overline{q'^2}\,\overline{w'^2}}\sqrt{\frac{\delta_w^2}{N\overline{w'^2}} + \frac{\delta_q^2}{N\overline{q'^2}}} \tag{A23}$$

$$\simeq \frac{1}{r}\overline{q'w'}\sqrt{\frac{\delta_w^2}{N\overline{w'^2}} + \frac{\delta_q^2}{N\overline{q'^2}}}$$

$$= \frac{1}{r}\overline{q'w'}\sqrt{\left(\frac{\delta_w^2}{\overline{w'^2}} + \frac{\delta_q^2}{\overline{q'^2}}\right)\frac{1}{N}}, \tag{A24}$$

where r is the correlation coefficient between vertical wind and water vapor fluctuations. The same equations hold for sensible heat fluxes replacing q' by θ'. Here, for low noise in the flux profiles, a large correlation coefficient and low relative noise error with respect to the atmospheric variances are important.

4) DISSIPATION AND MOLECULAR DESTRUCTION RATES

Finally, we derive the noise error for the dissipation rates based on Eqs. (47), (52), and (56). We achieve

$$\sigma_\varepsilon \simeq \varepsilon\sqrt{\frac{9}{4}\left(\frac{\sigma_{k_w}}{k_w}\right)^2 + \left(\frac{\sigma_U}{U}\right)^2}, \tag{A25}$$

$$\sigma_{\overline{N}_\theta} \simeq \overline{N}_\theta\sqrt{\left(\frac{\sigma_{k_\theta}}{k_\theta}\right)^2 + \frac{1}{4}\left(\frac{\sigma_{k_w}}{k_w}\right)^2 + \left(\frac{\sigma_U}{U}\right)^2}, \quad \text{and} \tag{A26}$$

$$\sigma_{\overline{N}_q} \simeq \overline{N}_q\sqrt{\left(\frac{\sigma_{k_q}}{k_q}\right)^2 + \frac{1}{4}\left(\frac{\sigma_{k_w}}{k_w}\right)^2 + \left(\frac{\sigma_U}{U}\right)^2}. \tag{A27}$$

In this case, σ_{k_w}, σ_{k_θ}, and σ_{k_q} are the errors in the determination of the fit coefficients to the structure function by the regression analysis, and σ_U is an error estimate for the horizontal wind profile.

REFERENCES

Ackerman, T. P., and G. M. Stokes, 2003: The Atmospheric Radiation Measurement Program—To predict reliably what increased greenhouse gases will do to global climate, we have to understand the crucial role of clouds. *Phys. Today*, **56**, 38–46, doi:10.1063/1.1554135.

Angevine, W., S. Avery, and G. Kok, 1993: Virtual heat flux measurements from a boundary-layer profiler-RASS compared to aircraft measurements. *J. Appl. Meteor.*, **32**, 1901–1907, doi:10.1175/1520-0450(1993)032<1901:VHFMFA>2.0.CO;2.

Ansmann, A., J. Fruntke, and R. Engelmann, 2010: Updraft and downdraft characterization with Doppler lidar: Cloud-free versus cumuli-topped mixed layer. *Atmos. Chem. Phys.*, **10**, 7845–7858, doi:10.5194/acp-10-7845-2010.

Ayotte, K. W., and Coauthors, 1996: An evaluation of neutral and convective planetary boundary-layer parameterizations relative to large eddy simulations. *Bound.-Layer Meteor.*, **79**, 131–175, doi:10.1007/BF00120078.

Behrendt, A., V. Wulfmeyer, A. Riede, G. Wagner, S. Pal, H. Bauer, M. Radlach, and F. Späth, 2009: Three-dimensional observations of atmospheric humidity with a scanning differential absorption Lidar. *Remote Sensing of Clouds and the Atmosphere XIV*, R. H. Picard, K. Schäfer, and A. Comeron et al., Eds., International Society for Optical Engineering (SPIE Proceedings, Vol. 7475), 74750L, doi:10.1117/12.835143.

——, and Coauthors, 2011: Observation of convection initiation processes with a suite of state-of-the-art research instruments during COPS IOP 8b. *Quart. J. Roy. Meteor. Soc.*, **137**, 81–100, doi:10.1002/qj.758.

——, E. Hammann, S. K. Muppa, S. Pal, and V. Wulfmeyer, 2015: Profiles of second- to forth-order moments of turbulent temperature fluctuations in the convective boundary layer: First measurements with rotational Raman lidar. *Atmos. Chem. Phys.*, **15**, 5485–5500, doi:10.5194/acp-15-5485-2015.

Cohn, S., and W. Angevine, 2000: Boundary layer height and entrainment zone thickness measured by lidars and wind-profiling radars. *J. Appl. Meteor.*, **39**, 1233–1247, doi:10.1175/1520-0450(2000)039<1233:BLHAEZ>2.0.CO;2.

Conzemius, R. J., and E. Fedorovich, 2006: Dynamics of sheared convective boundary layer entrainment. Part I: Methodological background and large-eddy simulations. *J. Atmos. Sci.*, **63**, 1151–1178, doi:10.1175/JAS3691.1.

Couvreux, F., F. Guichard, J.-L. Redelsperger, C. Kiemle, V. Masson, J.-P. Lafore, and C. Flamant, 2005: Water-vapour variability within a convective boundary-layer assessed by large-eddy simulations and IHOP_2002 observations. *Quart. J. Roy. Meteor. Soc.*, **131**, 2665–2693, doi:10.1256/qj.04.167.

——, ——, V. Masson, and J.-L. Redelsperger, 2007: Negative water vapour skewness and dry tongues in the convective boundary layer: Observations and large-eddy simulation budget analysis. *Bound.-Layer Meteor.*, **123**, 269–294, doi:10.1007/s10546-006-9140-y.

Crum, T., and R. Stull, 1987: Field measurements of the amount of surface layer air versus height in the entrainment zone. *J. Atmos. Sci.*, **44**, 2743–2753, doi:10.1175/1520-0469(1987)044<2743:FMOTAO>2.0.CO;2.

——, ——, and E. Eloranta, 1987: Coincident lidar and aircraft observations of entrainment into thermals and mixed layers. *J. Climate Appl. Meteor.*, **26**, 774–788, doi:10.1175/1520-0450(1987)026<0774:CLAAOO>2.0.CO;2.

Deardorff, J., 1970: A three-dimensional numerical investigation of the idealized planetary boundary layer. *Geophys. Fluid Dyn.*, **1**, 377–410, doi:10.1080/03091927009365780.

Dethloff, K., C. Abegg, A. Rinke, I. Hebestadt, and V. F. Romanov, 2001: Sensitivity of Arctic climate simulations to different boundary-layer parameterizations in a regional climate model. *Tellus*, **53A**, 1–26, doi:10.1034/j.1600-0870.2001.01073.x.

Emeis, S., 2011: *Surface-Based Remote Sensing of the Atmospheric Boundary Layer*. Atmospheric and Oceanographic Sciences Library, Vol. 40, Springer, 174 pp.

Fedorovich, E., R. Conzemius, and D. Mironov, 2004: Convective entrainment into a shear-free, linearly stratified atmosphere: Bulk models reevaluated through large eddy simulations. *J. Atmos. Sci.*, **61**, 281–295, doi:10.1175/1520-0469(2004)061<0281:CEIASL>2.0.CO;2.

Ferrare, R., and Coauthors, 2006: Evaluation of daytime measurements of aerosols and water vapor made by an operational Raman lidar over the Southern Great Plains. *J. Geophys. Res.*, **111**, D05S08, doi:10.1029/2005JD005836.

Frehlich, R., and L. Cornman, 2002: Estimating spatial velocity statistics with coherent Doppler lidar. *J. Atmos. Oceanic Technol.*, **19**, 355–366, doi:10.1175/1520-0426-19.3.355.

——, S. M. Hannon, and S. W. Henderson, 1998: Coherent Doppler lidar measurements of wind field statistics. *Bound.-Layer Meteor.*, **86**, 233–256, doi:10.1023/A:1000676021745.

Garcia, J. R., and J. P. Mellado, 2014: The two-layer structure of the entrainment zone in the convective boundary layer. *J. Atmos. Sci.*, **71**, 1935–1955, doi:10.1175/JAS-D-13-0148.1.

Giez, A., G. Ehret, R. L. Schwiesow, K. J. Davis, and D. H. Lenschow, 1999: Water vapor flux measurements from ground-based vertically pointed water vapor differential absorption and Doppler lidars. *J. Atmos. Oceanic Technol.*, **16**, 237–250, doi:10.1175/1520-0426(1999)016<0237:WVFMFG>2.0.CO;2.

Grachev, A. A., C. W. Fairall, and E. F. Bradley, 2000: Convective profile constants revisited. *Bound.-Layer Meteor.*, **94**, 495–515, doi:10.1023/A:1002452529672.

Hammann, E., A. Behrendt, F. Le Mounier, and V. Wulfmeyer, 2015: Temperature profiling of the atmospheric boundary layer with rotational Raman lidar during the HD(CP)^2 Observational Prototype Experiment. *Atmos. Chem. Phys.*, **15**, 2867–2881, doi:10.5194/acp-15-2867-2015.

Hechtel, L., C.-H. Moeng, and R. Stull, 1990: Temperature profiling of the atmospheric boundary layer with rotational Raman lidar during the HD(CP)^2 Observational Prototype Experiment. *J. Atmos. Sci.*, **47**, 1721–1741, doi:10.1175/1520-0469(1990)047<1721:TEONSF>2.0.CO;2.

Hill, K. A., and G. M. Lackmann, 2009: Analysis of idealized tropical cyclone simulations using the Weather Research and Forecasting Model: Sensitivity to turbulence parameterization and grid spacing. *Mon. Wea. Rev.*, **137**, 745–765, doi:10.1175/2008MWR2220.1.

Hogan, R. J., A. L. M. Grant, A. J. Illingworth, G. N. Pearson, and E. J. O'Connor, 2009: Vertical velocity variance and skewness in clear and cloud-topped boundary layers as revealed by Doppler lidar. *Quart. J. Roy. Meteor. Soc.*, **135**, 635–643, doi:10.1002/qj.413.

Hong, S.-Y., Y. Noh, and J. Dudhia, 2006: A new vertical diffusion package with an explicit treatment of entrainment processes. *Mon. Wea. Rev.*, **134**, 2318–2341, doi:10.1175/MWR3199.1.

Jiménez, P. A., J. Dudhia, J. F. González-Rouco, J. Navarro, J. P. Montávez, and E. García-Bustamante, 2012: A revised scheme for the WRF surface layer formulation. *Mon. Wea. Rev.*, **140**, 898–918, doi:10.1175/MWR-D-11-00056.1.

Kalthoff, N., and Coauthors, 2013: Dry and moist convection in the boundary layer over the Black Forest—A combined analysis of in situ and remote sensing data. *Meteor. Z.*, **22**, 445–461, doi:10.1127/0941-2948/2013/0417.

Kameyama, S., T. Ando, K. Asaka, Y. Hirano, and S. Wadaka, 2007: Compact all-fiber pulsed coherent Doppler lidar system for wind sensing. *Appl. Opt.*, **46**, 1953–1962, doi:10.1364/AO.46.001953.

Kanda, M., A. Inagaki, M. O. Letzel, S. Raasch, and T. Watanabe, 2004: LES study of the energy imbalance problem with eddy covariance fluxes. *Bound.-Layer Meteor.*, **110**, 381–404, doi:10.1023/B:BOUN.0000007225.45548.7a.

Kiemle, C., G. Ehret, A. Giez, K. Davis, D. Lenschow, and S. P. Oncley, 1997: Estimation of boundary layer humidity fluxes and statistics from airborne differential absorption lidar (DIAL). *J. Geophys. Res.*, **102**, 29 189–29 203, doi:10.1029/97JD01112.

——, and Coauthors, 2007: Latent heat flux profiles from collocated airborne water vapor and wind lidars during IHOP_2002. *J. Atmos. Oceanic Technol.*, **24**, 627–639, doi:10.1175/JTECH1997.1.

——, M. Wirth, A. Fix, S. Rahm, U. Corsmeier, and P. Di Girolamo, 2011: Latent heat flux measurements over complex terrain by airborne water vapour and wind lidars. *Quart. J. Roy. Meteor. Soc.*, **137**, 190–203, doi:10.1002/qj.757.

Kim, S.-W., S.-U. Park, and C.-H. Moeng, 2003: Entrainment processes in the convective boundary layer with varying wind shear. *Bound.-Layer Meteor.*, **108**, 221–245, doi:10.1023/A:1024170229293.

LeMone, M., 2002: Convective boundary layer. *Encyclopedia of Atmospheric Sciences*, 1st ed. J. Holton and J. Curry, Eds., Academic Press, 250–257.

Lenschow, D. H., J. Mann, and L. Kristensen, 1994: How long is long enough when measuring fluxes and other turbulence statistics? *J. Atmos. Oceanic Technol.*, **11**, 661–673, doi:10.1175/1520-0426(1994)011<0661:HLILEW>2.0.CO;2.

——, V. Wulfmeyer, and C. Senff, 2000: Measuring second-through fourth-order moments in noisy data. *J. Atmos. Oceanic Technol.*, **17**, 1330–1347, doi:10.1175/1520-0426(2000)017<1330:MSTFOM>2.0.CO;2.

——, M. Lothon, S. D. Mayor, P. P. Sullivan, and G. Canut, 2012: A comparison of higher-order vertical velocity moments in the convective boundary layer from lidar with in situ measurements and large-eddy simulation. *Bound.-Layer Meteor.*, **143**, 107–123, doi:10.1007/s10546-011-9615-3.

Linné, H., B. Hennemuth, J. Bösenberg, and K. Ertel, 2007: Water vapour flux profiles in the convective boundary layer. *Theor. Appl. Climatol.*, **87**, 201–211, doi:10.1007/s00704-005-0191-7.

Löhnert, U., D. D. Turner, and S. Crewell, 2009: Ground-based temperature and humidity profiling using spectral infrared and microwave observations. Part I: Simulated retrieval performance in clear-sky conditions. *J. Appl. Meteor. Climatol.*, **48**, 1017–1032, doi:10.1175/2008JAMC2060.1.

Lothon, M., D. H. Lenschow, and S. D. Mayor, 2006: Coherence and scale of vertical velocity in the convective boundary layer from a Doppler lidar. *Bound.-Layer Meteor.*, **121**, 521–536, doi:10.1007/s10546-006-9077-1.

——, ——, and ——, 2009: Doppler lidar measurements of vertical velocity spectra in the convective planetary boundary layer. *Bound.-Layer Meteor.*, **132**, 205–226, doi:10.1007/s10546-009-9398-y.

Maronga, B., and S. Raasch, 2013: Large-eddy simulations of surface heterogeneity effects on the convective boundary layer during the LITFASS-2003 experiment. *Bound.-Layer Meteor.*, **146**, 17–44, doi:10.1007/s10546-012-9748-z.

Mather, J. H., and J. W. Voyles, 2013: The ARM Climate Research Facility: A review of structure and capabilities. *Bull. Amer. Meteor. Soc.*, **94**, 377–392, doi:10.1175/BAMS-D-11-00218.1.

Matuura, M., Y. Masuda, H. Inuki, S. Kato, S. Fukao, T. Sato, and T. Tsuda, 1986: Radio acoustic measurement of temperature profile in the troposphere and stratosphere. *Nature*, **323**, 426–428, doi:10.1038/323426a0.

Mead, J., G. Hopcraft, S. Frasier, B. Pollard, C. Cherry, D. Schaubert, and R. McIntosh, 1998: A volume-imaging radar wind profiler for atmospheric boundary layer turbulence studies.

J. Atmos. Oceanic Technol., **15**, 849–859, doi:10.1175/1520-0426(1998)015<0849:AVIRWP>2.0.CO;2.

Milovac, J., K. Warrach-Sagi, J. Ingwersen, A. Behrendt, F. Späth, V. Wulfmeyer, and H. D. Wizemann, 2014: Sensitivity of the WRF model to boundary layer and land surface parameterizations: Comparisons with differential absorption lidar and eddy covariance measurements. *21st Symp. on Boundary Layers and Turbulence*, Leeds, United Kingdom, Amer. Meteor. Soc., 26. [Available online at https://ams.confex.com/ams/21BLT/webprogram/Paper248146.html.]

Moeng, C.-H., and P. P. Sullivan, 1994: A comparison of shear- and buoyancy-driven planetary boundary layer flows. *J. Atmos. Sci.*, **51**, 999–1022, doi:10.1175/1520-0469(1994)051<0999:ACOSAB>2.0.CO;2.

Monin, A. S., and A. Yaglom, 1975: *Statistical Fluid Mechanics*. Vol. 2, *Mechanics of Turbulence*, MIT Press, 896 pp.

Muppa, S. K., A. Behrendt, F. Späth, V. Wulfmeyer, S. Metzendorf, and A. Riede, 2015: Turbulent humidity fluctuations in the convective boundary layer: Case studies using water vapour differential absorption lidar measurements. *Bound.-Layer Meteor.*, doi:10.1007/s10546-015-0078-9, in press.

Muschinski, A., and P. Sullivan, 2013: Using large-eddy simulation to investigate intermittency fluxes of clear-air radar reflectivity in the atmospheric boundary layer. *Proc. Antennas and Propagation Society Int. Symp. (APSURSI)*, Orlando, FL, IEEE, 2321–2322, doi:10.1109/APS.2013.6711819.

Noh, Y., W. G. Cheon, S. Y. Hong, and S. Raasch, 2003: Improvement of the K-profile model for the planetary boundary layer based on large eddy simulation data. *Bound.-Layer Meteor.*, **107**, 401–427, doi:10.1023/A:1022146015946.

Pal, S., A. Behrendt, and V. Wulfmeyer, 2010: Elastic-backscatter-lidar-based characterization of the convective boundary layer and investigation of related statistics. *Ann. Geophys.*, **28**, 825–847, doi:10.5194/angeo-28-825-2010.

Park, S., and C. S. Bretherton, 2009: The University of Washington shallow convection and moist turbulence schemes and their impact on climate simulations with the Community Atmosphere Model. *J. Climate*, **22**, 3449–3469, doi:10.1175/2008JCLI2557.1.

Philippov, V., C. Codemard, Y. Jeong, C. Alegria, J. K. Sahu, J. Nilsson, and G. N. Pearson, 2004: High-energy in-fibre pulse amplification for coherent lidar applications. *Opt. Lett.*, **29**, 2590–2592, doi:10.1364/OL.29.002590.

Poulos, G. S., and Coauthors, 2002: CASES-99: A comprehensive investigation of the stable nocturnal boundary layer. *Bull. Amer. Meteor. Soc.*, **83**, 555–581, doi:10.1175/1520-0477(2002)083<0555:CACIOT>2.3.CO;2.

Saito, K., and Coauthors, 2013: Super high-resolution mesoscale weather prediction. *J. Phys.: Conf. Ser.*, **454**, 012073, doi:10.1088/1742-6596/454/1/012073.

Samuelsson, P., and Coauthors, 2011: The Rossby Centre Regional Climate model RCA3: Model description and performance. *Tellus*, **63A**, 4–23, doi:10.1111/j.1600-0870.2010.00478.x.

Senff, C., J. Bösenberg, and G. Peters, 1994: Measurement of water vapor flux profiles in the convective boundary layer with lidar and radar-RASS. *J. Atmos. Oceanic Technol.*, **11**, 85–93, doi:10.1175/1520-0426(1994)011<0085:MOWVFP>2.0.CO;2.

Sorbjan, Z., 1996: Effects caused by varying the strength of the capping inversion based on a large eddy simulation model of the shear-free convective boundary layer. *J. Atmos. Sci.*, **53**, 2015–2024, doi:10.1175/1520-0469(1996)053<2015:ECBVTS>2.0.CO;2.

——, 2001: An evaluation of local similarity on the top of the mixed layer based on large-eddy simulations. *Bound.-Layer Meteor.*, **101**, 183–207, doi:10.1023/A:1019260632125.

——, 2005: Statistics of scalar fields in the atmospheric boundary layer based on large-eddy simulations. Part I: Free convection. *Bound.-Layer Meteor.*, **116**, 467–486, doi:10.1007/s10546-005-0907-3.

——, 2006: Statistics of scalar fields in the atmospheric boundary layer based on large-eddy simulations. Part II: Forced convection. *Bound.-Layer Meteor.*, **119**, 57–79, doi:10.1007/s10546-005-9014-8.

——, 2009: Improving non-local parameterization of the convective boundary layer. *Bound.-Layer Meteor.*, **130**, 57–69, doi:10.1007/s10546-008-9331-9.

Späth, F., A. Behrendt, S. K. Muppa, S. Metzendorf, A. Riede, and V. Wulfmeyer, 2014: High-resolution atmospheric water-vapor measurements with a scanning differential absorption lidar. *Atmos. Chem. Phys. Discuss.*, **14**, 29 057–29 099, doi:10.5194/acpd-14-29057-2014.

Spuler, S. M., K. S. Repasky, B. Morley, D. Moen, M. Hayman, and A. R. Nehrir, 2015: Field-deployable diode-laser-based differential absorption lidar (DIAL) for profiling water vapor. *Atmos. Meas. Tech.*, **8**, 1073–1087, doi:10.5194/amt-8-1073-2015.

Stull, R. B., 1988: *An Introduction to Boundary Layer Meteorology*. Atmospheric and Oceanographic Sciences Library, Vol. 13, Springer, 670 pp.

Sullivan, P. P., C.-H. Moeng, B. Stevens, D. H. Lenschow, and S. D. Mayor, 1998: Structure of the entrainment zone capping the convective atmospheric boundary layer. *J. Atmos. Sci.*, **55**, 3042–3064, doi:10.1175/1520-0469(1998)055<3042:SOTEZC>2.0.CO;2.

Tatarski, V. I., 1961: *Wave Propagation in a Turbulent Medium*. McGraw-Hill, 285 pp.

Träumner, K., C. Kottmeier, U. Corsmeier, and A. Wieser, 2011: Convective boundary-layer entrainment: Short review and progress using Doppler lidar. *Bound.-Layer Meteor.*, **141**, 369–391, doi:10.1007/s10546-011-9657-6.

Tsuda, T., M. Miyamoto, and J. Furumoto, 2001: Estimation of a humidity profile using turbulence echo characteristics. *J. Atmos. Oceanic Technol.*, **18**, 1214–1222, doi:10.1175/1520-0426(2001)018<1214:EOAHPU>2.0.CO;2.

Tucker, S. C., W. A. Brewer, R. M. Banta, C. Senff, S. P. Sandberg, D. C. Law, A. M. Weickmann, and R. M. Hardesty, 2009: Doppler lidar estimation of mixing height using turbulence, shear, and aerosol profiles. *J. Atmos. Oceanic Technol.*, **26**, 673–688, doi:10.1175/2008JTECHA1157.1.

Turner, D. D., and J. E. M. Goldsmith, 1999: Twenty-four-hour Raman lidar water vapor measurements during the Atmospheric Radiation Measurement Program's 1996 and 1997 water vapor intensive observation periods. *J. Atmos. Oceanic Technol.*, **16**, 1062–1076, doi:10.1175/1520-0426(1999)016<1062:TFHRLW>2.0.CO;2.

——, and U. Löhnert, 2014: Information content and uncertainties in thermodynamic profiles and liquid cloud properties retrieved from the ground-based Atmospheric Emitted Radiance Interferometer (AERI). *J. Appl. Meteor. Climatol.*, **53**, 752–771, doi:10.1175/JAMC-D-13-0126.1.

——, R. A. Ferrare, L. A. Heilman Brasseur, W. F. Feltz, and T. P. Tooman, 2002: Automated retrievals of water vapor and aerosol profiles over Oklahoma from an operational Raman lidar. *J. Atmos. Oceanic Technol.*, **19**, 37–50, doi:10.1175/1520-0426(2002)019<0037:AROWVA>2.0.CO;2.

——, ——, V. Wulfmeyer, and A. J. Scarino, 2014a: Aircraft evaluation of ground-based Raman lidar water vapor turbulence profiles in convective mixed layers. *J. Atmos. Oceanic Technol.*, **31**, 1078–1088, doi:10.1175/JTECH-D-13-00075.1.

——, V. Wulfmeyer, L. K. Berg, and J. H. Schween, 2014b: Water vapor turbulence profiles in stationary continental convective

mixed layers. *J. Geophys. Res. Atmos.*, **119**, 11 151–11 165, doi:10.1002/2014JD022202.

Van Zanten, M. C., P. G. Duynkerke, and J. W. M. Cuijpers, 1999: Entrainment parameterization in convective boundary layers. *J. Atmos. Sci.*, **56**, 813–828, doi:10.1175/1520-0469(1999)056<0813:EPICBL>2.0.CO;2.

Waggy, S. B., S. Biringen, and P. Sullivan, 2013: Direct numerical simulation of top-down and bottom-up diffusion in the convective boundary layer. *J. Fluid Mech.*, **724**, 581–606, doi:10.1017/jfm.2013.130.

Wulfmeyer, V., 1999a: Investigation of turbulent processes in the lower troposphere with water vapor DIAL and radar-RASS. *J. Atmos. Sci.*, **56**, 1055–1076, doi:10.1175/1520-0469(1999)056<1055:IOTPIT>2.0.CO;2.

——, 1999b: Investigations of humidity skewness and variance profiles in the convective boundary layer and comparison of the latter with large eddy simulation results. *J. Atmos. Sci.*, **56**, 1077–1087, doi:10.1175/1520-0469(1999)056<1077:IOHSAV>2.0.CO;2.

——, and T. Janjić, 2005: Twenty-four-hour observations of the marine boundary layer using shipborne NOAA high-resolution Doppler lidar. *J. Appl. Meteor.*, **44**, 1723–1744, doi:10.1175/JAM2296.1.

——, and Coauthors, 2008: The Convective and Orographically Induced Precipitation Study: A research and development project of the World Weather Research Program for improving quantitative precipitation forecasting in low-mountain regions. *Bull. Amer. Meteor. Soc.*, **89**, 1477–1486, doi:10.1175/2008BAMS2367.1.

——, S. Pal, D. D. Turner, and E. Wagner, 2010: Can water vapour Raman lidar resolve profiles of turbulent variables in the convective boundary layer? *Bound.-Layer Meteor.*, **136**, 253–284, doi:10.1007/s10546-010-9494-z.

——, and Coauthors, 2011: The Convective and Orographically-induced Precipitation Study (COPS): The scientific strategy, the field phase, and first highlights. *Quart. J. Roy. Meteor. Soc.*, **137**, 3–30, doi:10.1002/qj.752.

——, and Coauthors, 2015a: A review of the remote sensing of lower tropospheric thermodynamic profiles and its indispensable role for the understanding and the simulation of water and energy cycles. *Rev. Geophys.*, **53**, 819–895, doi:10.1002/2014RG000476.

——, and Coauthors, 2015b: New concepts for studying land-surface-atmosphere feedback based on a new lidar synergy and grey zone simulations. *Geophysical Research Abstracts*, Vol. 17, Abstract EGU2015-5054. [Available online at http://meetingorganizer.copernicus.org/EGU2015/EGU2015-5054.pdf.]

Wyngaard, J. C., and R. A. Brost, 1984: Top-down and bottom-up diffusion of a scalar in the convective boundary layer. *J. Atmos. Sci.*, **41**, 102–112, doi:10.1175/1520-0469(1984)041<0102:TDABUD>2.0.CO;2.

Xie, B., J. C. H. Fung, A. Chan, and A. Lau, 2012: Evaluation of nonlocal and local planetary boundary layer schemes in the WRF model. *J. Geophys. Res.*, **117**, D12103, doi:10.1029/2011JD017080.

Zehe, E., and Coauthors, 2014: From response units to functional units: A thermodynamic reinterpretation of the HRU concept to link spatial organization and functioning of intermediate scale catchments. *Hydrol. Earth Syst. Sci.*, **18**, 4635–4655, doi:10.5194/hess-18-4635-2014.

Zhou, M. Y., D. H. Lenschow, B. B. Stankov, J. C. Kaimal, and J. E. Gaynor, 1985: Wave and turbulence structure in a shallow baroclinic convective boundary layer and overlying inversion. *J. Atmos. Sci.*, **42**, 47–57, doi:10.1175/1520-0469(1985)042<0047:WATSIA>2.0.CO;2.